JVST A
Journal of Vacuum Science & Technology A

Ion implantation in β-Ga_2O_3: Physics and technology

Cite as: J. Vac. Sci. Technol. A **39**, 030802 (2021); https://doi.org/10.1116/6.0000928
Submitted: 15 January 2021 • Accepted: 04 March 2021 • Published Online: 26 March 2021

Alena Nikolskaya, Evgenia Okulich, Dmitry Korolev, et al.

COLLECTIONS

Paper published as part of the special topic on Gallium Oxide Materials and Devices

F This paper was selected as Featured

ARTICLES YOU MAY BE INTERESTED IN

A review of Ga_2O_3 materials, processing, and devices
Applied Physics Reviews **5**, 011301 (2018); https://doi.org/10.1063/1.5006941

Recent progress on the electronic structure, defect, and doping properties of Ga_2O_3
APL Materials **8**, 020906 (2020); https://doi.org/10.1063/1.5142999

Gallium oxide (Ga_2O_3) metal-semiconductor field-effect transistors on single-crystal β-Ga_2O_3 (010) substrates
Applied Physics Letters **100**, 013504 (2012); https://doi.org/10.1063/1.3674287

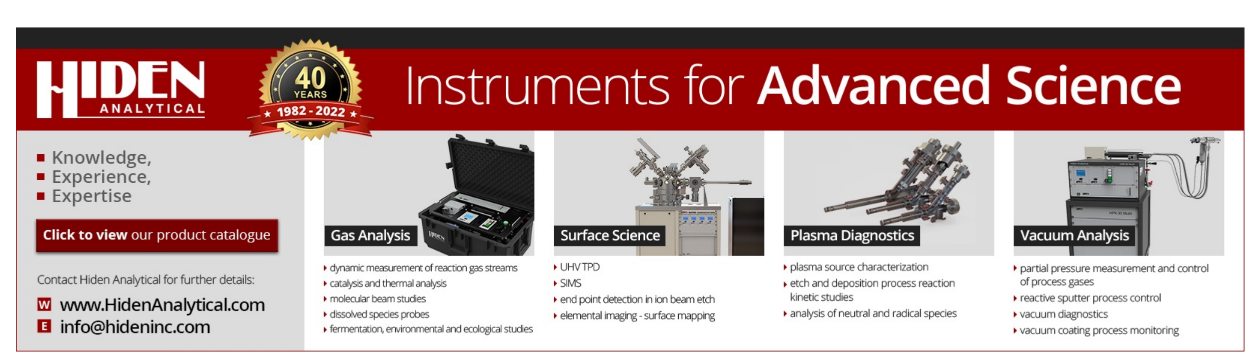

© 2021 Author(s).

REVIEW

avs.scitation.org/journal/jva

Ion implantation in β-Ga_2O_3: Physics and technology

Cite as: J. Vac. Sci. Technol. A **39**, 030802 (2021); doi: 10.1116/6.0000928
Submitted: 15 January 2021 · Accepted: 4 March 2021 ·
Published Online: 26 March 2021

View Online

Export Citation

CrossMark

Alena Nikolskaya,[1] Evgenia Okulich,[1] Dmitry Korolev,[1] Anton Stepanov,[2] Dmitry Nikolichev,[1] Alexey Mikhaylov,[1] David Tetelbaum,[1] Aleksei Almaev,[3] Charles Airton Bolzan,[4] Antônio Buaczik, Jr.,[4] Raquel Giulian,[4] Pedro Luis Grande,[4] Ashok Kumar,[5] Mahesh Kumar,[5] and Daniela Gogova[1,6,a)]

AFFILIATIONS

[1]Research Institute of Physics and Technology, Lobachevsky University, Nizhny Novgorod 603950, Russia
[2]Chuvash State Agricultural Academy, Cheboksary 428017, Russia
[3]Research and Development Center for Advanced Technologies in Microelectronics, Tomsk State University, Tomsk 634050, Russia
[4]Ion Implantation Laboratory, Institute of Physics—Federal University of Rio Grande do Sul, Porto Alegre 91501-970, Brazil
[5]Department of Electrical Engineering, Indian Institute of Technology Jodhpur, Jodhpur 342037, India
[6]Centre for Materials Science and Nanotechnology, University of Oslo, Blindern, 0316 Oslo, Norway

Note: This paper is part of the Special Topic Collection on Gallium Oxide Materials and Devices.
[a)]**Electronic mail:** daniela.gogova-petrova@smn.uio.no

ABSTRACT

Gallium oxide, and in particular its thermodynamically stable β-Ga_2O_3 phase, is within the most exciting materials in research and technology nowadays due to its unique properties. The very high breakdown electric field and the figure of merit rivaled only by diamond have tremendous potential for the next generation "green" electronics enabling efficient distribution, use, and conversion of electrical energy. Ion implantation is a traditional technological method used in these fields, and its well-known advantages can contribute greatly to the rapid development of physics and technology of Ga_2O_3-based materials and devices. Here, the status of ion implantation in β-Ga_2O_3 nowadays is reviewed. Attention is mainly paid to the results of experimental study of damage under ion irradiation and the properties of Ga_2O_3 layers doped by ion implantation. The results of *ab initio* theoretical calculations of the impurities and defect parameters are briefly presented, and the physical principles of a number of analytical methods used to study implanted gallium oxide layers are highlighted. The use of ion implantation in the development of Ga_2O_3-based devices, such as metal oxide field-effect transistors, Schottky barrier diodes, and solar-blind UV detectors, is described together with systematical analysis of the achieved values of their characteristics. Finally, the most important challenges to be overcome in this field of science and technology are discussed.

Published under license by AVS. https://doi.org/10.1116/6.0000928

I. INTRODUCTION

Gallium oxide (Ga_2O_3) is an ultrawide bandgap semiconductor that has attracted enormous attention from the research community in the field of electronics and optoelectronics. The history of research on this material goes back over more than 60 years, but only recently it has acquired the reputation of the main candidate for the next generation "green" power electronics able to provide efficient distribution, use, and conversion of electrical energy for sustainable development.

Initially, researchers focused their attention on wide bandgap materials such as SiC and GaN. However, the situation has changed after the demonstration of high-quality power field-effect transistors on the basis of β-Ga_2O_3, which is the most stable modification within the various polymorphs of gallium oxide. Since then, the number of publications devoted to Ga_2O_3 has a steep surge (Fig. 1), including several review articles.[1–7]

The main advantages of this attractive material are the following:

(i) the wide bandgap (4.5–4.9 eV) and the very high breakdown electric field value (about 8 MeV/cm, according to theoretical calculations), which is larger than the corresponding values

Published under license by AVS.

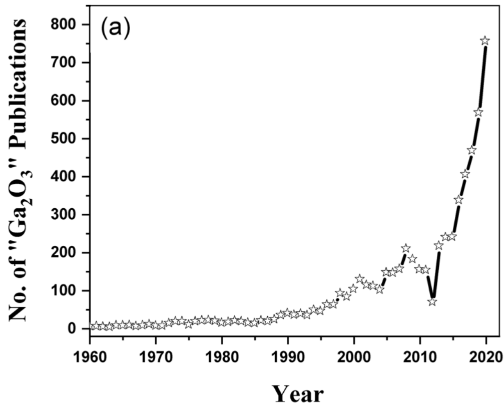

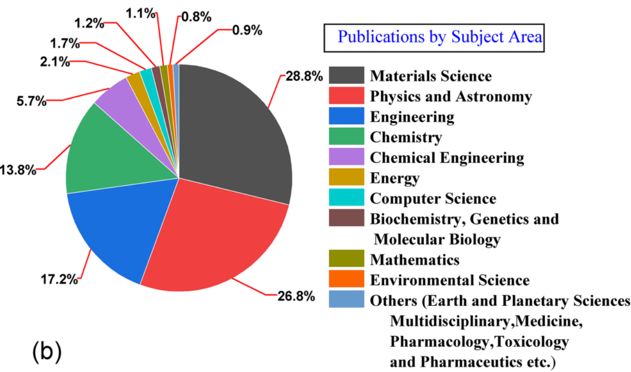

FIG. 1. Number of publications on Ga_2O_3 from 1960 to 2020 (a) and their distribution over subject areas (b). The papers were searched with the criterion of containing "Ga_2O_3" in the title (Data: Scopus).

of SiC and group III-nitride semiconductor compounds (GaN, AlN, InN, and alloys),

(ii) radiation hardness and chemical resistance, allowing the devices to remain operational under conditions of ionizing radiation and in aggressive environment, and

(iii) existence of cost-effective melt growth techniques for large-diameter ingots in comparison with the expensive methods of SiC, AlN, and GaN bulk crystals growth.

It is well known that electronics has reached great success thanks to the development of ion implantation as a key method in processing of practically all semiconductor devices. The main advantages of this method include (1) the precise dosage of dopants, (2) ability to control the spatial distribution of dopants and to use radiation defects generated by ion irradiation to modify the material properties—"defect engineering," and (3) relatively low temperatures required for the implantation-related technology. All these advantages and a number of other useful features of the ion implantation can be exploited to enhance the potential of gallium oxide in device applications. The significance of ion implantation additionally increases due to the well-known problem of obtaining Ga_2O_3 *p*-type conductivity under growth conditions close to thermodynamic equilibrium. The ion implantation as a nonequilibrium method seems to be a promising approach to overcome this challenge.

Investigations on Ga_2O_3 ion implantation have begun quite recently, and only a relatively small circle of fundamental or applied problems has been faced so far. Nevertheless, the advantages of this method have already been demonstrated for a number of important practical applications. In particular, the possibility of significant improvement in the properties of ohmic contacts by ion doping is established, which makes it possible to enhance the operating parameters of some semiconductor devices. It is also important that the possibility of a controlled increase in the resistivity of n-Ga_2O_3 by ion doping with some acceptor impurities and radiation defects incorporation is discovered. New approaches are developed for the ion synthesis and ion modification of Ga_2O_3 nanostructures for optoelectronic devices. Meanwhile, successful developments in material science and engineering are impossible without theoretical modeling. For research in the area of ion implantation, it is necessary to use the results of computer calculations regarding the influence of impurities and point defects on the electronic structure and properties of β-Ga_2O_3.

This article is devoted to a systematical review of the main published results in the field of β-Ga_2O_3 ion implantation.

The review is organized as follows. After Sec. I, the main results of computer simulations of the electronic structure of β-Ga_2O_3 with dopants and defects are surveyed (Sec. II). Section III describes the characterization methods employed in the experiments with ion implantation of Ga_2O_3. This section is intended predominantly for readers who are not experts in materials characterization. In Sec. IV, the properties of impurities introduced in β-Ga_2O_3 by ion implantation are examined. Then, the features of defect formation upon Ga_2O_3 irradiation with ions of different masses and energies are briefly reviewed. In Sec. V, both scientific and applied aspects related to the development of Ga_2O_3-based electronic and optoelectronic devices are highlighted. In Sec. VI, a general assessment of the state-of-the-art in the field of ion implantation in β-Ga_2O_3 and the main challenges to be addressed in this field are given.

II. THEORETICAL CALCULATIONS

The study of physical foundations of ion implantation is generally aimed to solve the following three problems: (a) radiation defects: their nature, regularities of formation and annealing, distributions, diffusion rates, and influence on the properties of implanted layers; (b) ion doping regularities: the implanted impurities activation processes, energy levels, diffusion rates, distributions, and influence on electrical, optical and other properties; (c) defect-impurity interaction: the influence of interaction on the diffusion rates and on the implanted layer properties. The term "defects," where this does not lead to confusion, will be used below to denote exactly both defects and impurities.

Although the modern arsenal of experimental methods provides rich opportunities for solving the mentioned problems, some of them often cannot be reliably solved without theoretical consideration, especially without *ab initio* methods. Among such

problems are the identification of defects and impurities responsible for one or other experimentally found energy levels and explanation of the observed properties.

At present, almost all *ab initio* calculations are limited to the consideration of elementary entities—vacancies, interstitials, single impurity atoms, and some simple complexes. Of course, for ion implantation, the list of formed defect types is significantly greater and includes complicated complexes, extended defects, disordered nanoregions, etc. However, in some cases, e.g., upon irradiation with light ions at not too high doses, mainly the same types of defects are present as those introduced during crystal growth or epitaxy. Thus, the knowledge of theoretical approaches and the results of corresponding calculations are very desirable for researchers dealing with ion implantation in Ga_2O_3.

The *ab initio* approach most often used to study β-Ga_2O_3 materials is the so-called density-function theory (DFT). The basics of the approach are considered, for example, in Refs. 8 and 9. For a wide bandgap semiconductor (with expressed ionic type of atomic bonding), there are some peculiarities that need to be taken into account when using this approach. Thus, the standard local density approximation and the semilocal generalized gradient approximation (GGA) are not well adequate.[10] In modern works, to take into account these peculiarities, the so-called hybrid exchange-density functional is used.[11,12] For β-Ga_2O_3, this is the HSE06 functional.[13–17] The choice of optimal parameters included in the HSE06 functional is proposed in Ref. 10, although some other parameters are used too. The alternative *ab initio* approach is the (GGA + U) with exchange-correlation energy Perdew-Burke-Ernzerhof (PBE).[18]

The DFT-calculated values of levels formed for typical defects and impurities in β-Ga_2O_3, as well as respective experimental data, are presented in Table I. The data of different theoretical works do not always agree with each other due to the difference in the parameters used, and, in some cases, because of the different calculation methods. However, the qualitative conclusions drawn by different authors are generally identical.

The comparison of the calculated and experimental values of the levels is only possible if they are correctly attributed to one or other entities. Authors of experimental works usually justify their attribution by the proximity of the found values of levels to one or other theoretically calculated values. However, optical or electrical methods do not allow direct attribution by themselves. In cases where defects and impurities are introduced during growth, the attribution problem is facilitated by the fact that the resulting state is often (although not always) close to thermodynamic equilibrium, so it is possible to take into account the calculated quantity of the defect formation energies: the smaller the formation energy, the more energetically favorable the formation of a given defect is. However, in the case of ion implantation, the state of implanted layers is generally far from equilibrium. Although the system approaches equilibrium upon annealing, the degree of approach strongly depends on the implantation and annealing conditions and is not always known. Thus, for ion implantation, the attribution of defects is a more difficult task and requires some additional assumptions, including the estimation of kinetic factors (see, e.g., Ref. 21).

In addition to defects and impurities, the DFT method was used to calculate the energy levels of the so-called "self-trapped holes (STH)." STH appears when the free hole state (in the valence band) is less energetically favorable than for its localization near some lattice positions.[16] For β-Ga_2O_3, according to calculations, these positions are localized near the oxygen atoms.[16] These atoms OI, OII, and OIII occupy three nonequivalent positions in the unit/cell (Fig. 2), and correspondingly STH levels in the bandgap are created (although some of them, as shown in Ref. 27, may be unstable). The localization of a hole at the STH level causes a strong distortion of the lattice in its vicinity that leads to the formation of the so-called small polaron,[33] which, according to the calculations,[16] has an extremely low mobility. This circumstance is considered one (but not single) of the main challenges on the way to *p*-type β-Ga_2O_3. The existence of STH in β-Ga_2O_3 was confirmed in Ref. 32 by the photoluminescence (PL) method with polarized light excitation. The STH levels were calculated by DFT[10,16,27,32] and found in the experimental work.[34]

First-principal calculations were also used to calculate the migration energies of defects and impurities in β-Ga_2O_3. Thus, in Ref. 35, the barriers for migration of V_O^{2+} and V_O^0 were calculated to be 1.8 and 2.6 eV, respectively. For V_{Ga}, lower barrier values were obtained[35] and a conclusion was drawn about their higher mobility at low temperatures, compared to V_O. In Ref. 30, the energies of Mg migration over interstitial sites (from 0.56 to 0.75 eV) and migration of N over oxygen vacancies (3.87 eV) were calculated.

The results presented here show that the theoretical study on defects and impurities in β-Ga_2O_3 requires further development and experimental verification. In particular, it is not entirely clear which value of ϵ (ϵ_0 or ϵ_∞) gives a more accurate result when using the HSE functional. With increase in the size of computational cell, the results calculated with ϵ_0 apparently will become more reliable, but this increase will require a significant elevation in the computer resources. One more question is also not entirely resolved: which of the two approaches (HSE or GGA + U) provides the best agreement with the experimental data. Nevertheless, already at the present stage, the use of theoretical calculations in the interpretation of experimental results is very useful and often it is mandatory.

III. ANALYTICAL METHODS

The analytical methods typically used in Ga_2O_3 study are discussed below.

A. Transmission electron microscopy

Transmission electron microscopy (TEM) serves to study the crystalline structure and defects of thin films or thinned layers of bulk samples.[36] This very powerful method is based on the use of dual—corpuscular and wave—nature of electrons. The electrons of the parallel incident beam passing through the sample (with energies usually of the order of several hundred keV) undergo diffraction on the crystal lattice (coherent scattering) and/or incoherent scattering on atoms. Transmitted and scattered electrons are controlled using electronic lens systems and variable aperture

Published under license by AVS.

TABLE I. Values of DFT-calculated and experimentally found energy levels of defects, impurities, and STHs. E_C–conduction band edge; E_V–valence band edge; $\epsilon_0 \approx 10$–static dielectric constant; $\epsilon_\infty \approx 3.55$–high frequency dielectric constant; ϵ_{calc}–calculated dielectric tensor; V–vacancy; GaI, GaII, OI, OII, OIII correspond to different lattice positions of Ga and O atoms (Fig. 2), STH_{OI}, STH_{OII}, and STH_{OIII} correspond to the positions of trapped hole (at respective O atoms). The designation of the kind of defects and STH are placed opposite to the first line of data related to a given kind.

Kind of defects, impurities and STH	Charge transitions	Energy levels (eV)	Kind of DFT, dielectric constant used	Reference	Experimental values (eV) (technique used)
V_{GaI}	−2/−3	$E_C - 0.67$	HSE, ϵ_∞	Ref. 10	$E_C - 0.74$ (DLTS) Ref. 19 $E_C - 0.82$ (DLTS) Ref. 20
		$E_C - 1.62$	HSE, ϵ_0	Ref. 15	
		$E_C - 1.76$	HSE, ϵ_0	Ref. 21	
		$E_C - 0.69$	HSE, ϵ_∞		
		$E_C - 2.27$	$\epsilon = 12.7$	Ref. 22	
V_{GaII}	−2/−3	$E_C - 1.16$	HSE, ϵ_∞	Ref. 10	$E_C - 1.04$ (DLTS) Ref. 19 $E_C - 1.00$ (DLTS) Ref. 20
		$E_C - 1.83$	HSE, ϵ_0	Ref. 15	
		$E_C - 1.93$	$\epsilon = 12.7$	Ref. 22	
		$E_C - 2.17$	HSE, ϵ_0	Ref. 21	
		$E_C - 1.11$	HSE, ϵ_∞		
V_{OI}	+2/0	$E_C - 2.10$	HSE, ϵ_∞	Ref. 10	
		$E_C - 1.52$	HSE, ϵ_0	Ref. 17	
		$E_C - 1.72$	PBE, (GGA + U) approach	Ref. 23	
		$E_C - 1.50$	HSE, ϵ_0	Ref. 21	
V_{OII}	+2/0	$E_C - 2.68$	HSE, ϵ_∞	Ref. 10	
		$E_C - 2.29$	HSE, ϵ_0		$E_C - 2.16$ (DLOS) Ref. 20
		$E_C - 2.16$	HSE, ϵ_0	Ref. 17	
		$E_C - 2.42$	$\epsilon = 12.7$	Ref. 22	
		$E_C - 1.22$	PBE, (GGA + U) approach	Ref. 23	$E_C - 1.40$ (PL) Ref. 23
		$E_C - 2.23$	HSE, ϵ_0	Ref. 21	
V_{OIII}	+2/0	$E_C - 1.95$	HSE, ϵ_∞	Ref. 10	
		$E_C - 1.26$	HSE, ϵ_0	Ref. 17	
		$E_C - 1.02$	PBE, (GGA + U) approach	Ref. 23	
		$E_C - 1.36$	HSE, ϵ_0	Ref. 21	
		$E_C - 1.79$	HSE, ϵ_∞	Ref. 21	
Mg_{GaI}	0/−1	$E_V + 1.25$		Ref. 24	
		$E_V + 1.27$	HSE, ϵ_0	Ref. 25	
		$E_V + 1.62$		Ref. 26	
		$E_V + 1.30$		Ref. 27	
Mg_{GaII}	0/−1	$E_V + 1.05$		Ref. 24	$E_V + 1.1$ (conductivity) Ref. 28
		$E_V + 1.06$	HSE, ϵ_0	Ref. 25	
		$E_V + 1.25$	HSE, ϵ_0	Ref. 29	

Published under license by AVS.

TABLE I. (*Continued.*)

Kind of defects, impurities and STH	Charge transitions	Energy levels (eV)	Kind of DFT, dielectric constant used	Reference	Experimental values (eV) (technique used)
		$E_V + 1.57$		Ref. 26	
		$E_V + 1.40$		Ref. 27	
		$E_V + 1.40$		Ref. 30	
N_{OI}	0/−1	$E_V + 3.50$	HSE, ϵ_0	Ref. 29	
		$E_V + 3.50$		Ref. 27	
		$E_V + 3.40$		Ref. 30	
N_{OII}	0/−1	$E_V + 3.40$	HSE, ϵ_0	Ref. 29	
		$E_V + 2.20$		Ref. 27	
		$E_V + 3.50$		Ref. 30	
N_{OIII}	0/−1	$E_V + 2.20$	HSE, ϵ_0	Ref. 29	
		$E_V + 3.40$		Ref. 27	
		$E_V + 2.20$		Ref. 30	
V_{GaI}-H	+1/0	$E_C - 0.89$		Ref. 31	
	0/−1	$E_C - 1.53$			
	−1/−2	$E_C - 2.21$			
		$E_C - 1.93$		Ref. 15	
V_{GaI}-2H	+1/0	$E_C - 1.90$		Ref. 31	
	0/−1	$E_C - 1.64$			
	−1/−2	$E_C - 1.77$			
V_{GaII}-3H	+1/0	$E_C - 1.28$		Ref. 31	
	0/−1	$E_C - 1.15$			
	−1/−2	$E_C - 2.25$			
Fe_{GaI}	0/−1	$E_C - 0.59$		Ref. 21	
STH_{OI}	+1/0	$E_V + 0.58$	HSE, ϵ_{calc}	Ref. 27	
		$E_C - 4.61$	HSE, ϵ_∞	Ref. 10	
		$E_V + 1.02$	pSIC + PBE-GGA	Ref. 32	
STH_{OII}	+1/0	$E_C - 4.50$	HSE, ϵ_∞	Ref. 10	
		$E_V + 1.02$	pSIC + PBE-GGA	Ref. 32	
STH_{OIII}	+1/0	$E_V + 0.58$	HSE, ϵ_{calc}	Ref. 27	

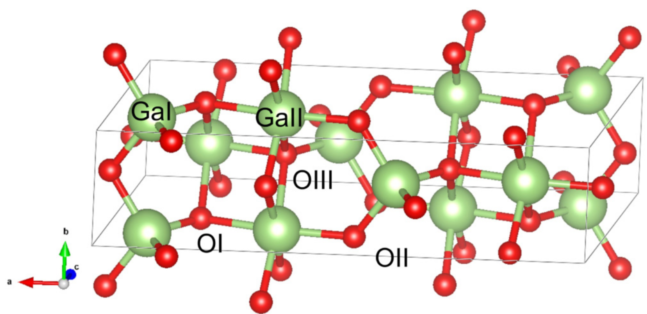

FIG. 2. Unit cell of β-Ga_2O_3. Figures I, II, and III indicate different types of Ga and O sites. GaI and OIII are tetrahedrally, GaII–octahedrally, OI and OII–trigonally coordinated atoms.

diaphragms (Fig. 3). So, the images and the diffraction pattern for the selected area of a sample can be formed.

The diffraction mode allows determining the nature of the crystalline structure of the sample studied and identifying the material by comparison with reference data. A single-crystalline material forms a system of point reflections, a polycrystalline one—a system of narrow rings, and an amorphous film forms a halo or a few numbers of wide rings.

As electrons pass through the sample, some of the electrons undergo coherent and incoherent scattering, which makes it possible to implement two modes of imaging: bright field (BF) and dark field (DF). In the first mode, the aperture diaphragm of the objective lens (Fig. 3) transmits the electrons of the incident beam. In this case, areas with a greater thickness or containing heavier chemical elements look darker due to the larger proportion of scattered electrons. Amorphous inclusions against the crystalline areas will also

Published under license by AVS.

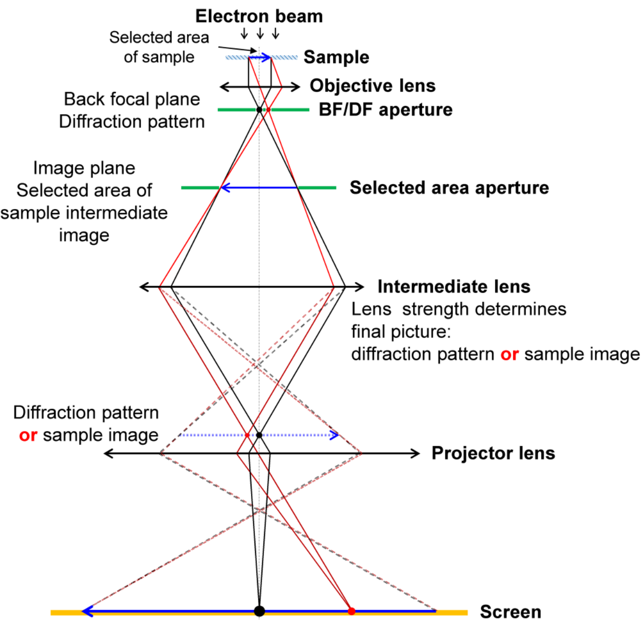

FIG. 3. Diagram of the rays in two basic modes of TEM. Deflection angles in the figure are much larger than real ones (for better understanding). Only necessary lenses and apertures are shown; the real TEM has many more (that gives more flexible control). Intermediate lens changes the final picture on the screen (the ray's ways after this lens split on two: solid lines are for diffraction pattern; dotted lines are for image of the sample). BF/DF apertures are used for the corresponding mode choice. *Selected area aperture* is used to limit the area from which the diffraction pattern is obtained.

look darker due to a strong incoherent scattering. For polycrystalline thin films, the grains having different orientations will differ in brightness due to the difference in the fraction of electrons involved in the coherent (Bragg) scattering. In the DF mode, the image of the crystalline sample is built using the selected diffracted beams (with a DF aperture), while the transmitted beam does not participate in the image formation. This mode, in particular, allows visualization of a second phase inclusions and to obtain contrast images of crystalline inclusions in an amorphous material.

Scanning a sample by a very sharp (less than 0.1 nm in diameter) focused electron beam makes it possible to implement the high angle annular dark field image mode. For this mode, an image is formed by those electrons that have been deflected (as a result of incoherent scattering) at such a large angle that coherent scattering no longer makes a significant contribution to the signal. Then, the regions with a less perfect structure appear brighter compared to the surrounding regions.

Another image mode can be realized at high magnifications ($>10^6$)—high-resolution transmission electron microscopy (HRTEM). In this mode, the interference of the diffracted beams with the primary one creates periodic lines corresponding to atomic planes. Measuring the distances between the lines allows us to find the interplanar distances and thus to identify the observed phases. The Fourier transform of the image often facilitate to create such reflections, which are not seen on the diffraction picture due to their low intensity. HRTEM is a very powerful method in revealing extended defects such as dislocations, stacking faults, and twin boundaries.

B. Scanning electron microscopy

Scanning electron microscopy (SEM) is based on the registration of electrons outgoing from the sample surface during its irradiation by a scanning focused electron beam with a typical energy of several tens of keV. There are two main modes of SEM. In one of them, a current caused by secondary electrons (SE) is recorded. The SE are generated in the near-surface layer of the sample investigated due to the interaction of the beam with weakly bound electrons localized on the atomic shells and/or in the valence band of the semiconductor. The coefficient of SE emission depends on the local angle between the surface and the beam. Thus, by using beam scanning and registering the SE current, the surface morphology can be observed. Thereby, computer graphics allows creating its three-dimensional image.

In another SEM mode called backscattering electrons (BSE), the yield of electrons elastically scattered from the sample surface is recorded. The BSE yield depends on the mass of the target atoms. This makes it possible to investigate by scanning the degree of compositional homogeneity of the sample surface layer.

In addition to SE and BSE modes, modern scanning electron microscopes are equipped with facilities for recording signals such as Auger electron emission, characteristic secondary x rays, electron beam induced current (EBIC), and cathodoluminescence (CL).

SEM can be used both in plan-view geometry and in cross section of the samples. This, in particular, allows one to visualize and investigate the interval boundaries of various phases, including those formed by ion implantation.

C. Energy dispersive spectroscopy

Energy dispersive spectroscopy (EDS) is based on the detection of characteristic x-ray emission under an electron beam and is used in analytical electron microscopy. It allows exploring the elemental composition of near-surface layers of samples together with TEM and SEM images, surface morphology, and other local characteristics. This method is particularly useful for the identification of nano-objects observed by these techniques. The typical thickness of the probed layer is from several units to several tens of micrometers. EDS is often used to determine the distribution of elemental composition (elemental maps) over depth by probing the cross section of a sample.

D. X-ray diffraction

To study the structure of implanted Ga_2O_3 layers, x-ray diffraction (XRD) is most often used. If a monochromatic x-ray beam is directed at an angle θ to some family of atomic planes, a diffracted beam occurs under the condition

$$2d \sin \theta = n\lambda, \tag{1}$$

where d is the interplanar distance, λ is the wavelength, and n is an integer (the diffraction order). XRD allows one to obtain several basic characteristics of the investigated samples as follows:

Published under license by AVS.

(1) If the phase composition of the sample is not known in advance, then it can be identified using the values of θ at which the diffraction maxima are observed.
(2) The method makes it possible to establish whether the analyzed layer of the sample has a single-crystalline, polycrystalline, or amorphous structure. In the first case, in the set of diffraction peaks recorded with variation of the angle θ, there are only those that correspond to different values of n for the same family of atomic planes; in the second case, the peaks corresponding to different families of planes are observed; in the third case, usually there are no peaks at all.
(3) The intensity and width of the peaks are used to judge the degree of structural perfection of single-crystalline layers. For this purpose, a high-resolution x-ray diffraction (HRXRD) is used with an angular resolution of the order of a few angle seconds.
(4) The value of the shift of the XRD peak positions versus the reference peak positions are used to determine the changes in the lattice parameters associated with the presence of the impurities and defects.
(5) In HRXRD, the presence, character, and magnitude of strain in single-crystalline layers, in particular, those modified by ion irradiation, can be determined from the diffraction peaks positions.

In the case of using XRD to study layers modified by ion implantation, the analysis of data can be complicated when the thickness of the analyzed layer is significantly larger than the depth of ion penetration, as well as when a gradient of parameters over depth takes place. (The effect of this factor can be reduced by using small angles between the sample surface and the incident beam.)

E. X-ray absorption fine structure

This method includes two modes: x-ray absorption near edge spectroscopy (XANES) and extended x-ray absorption fine structure (EXAFS). In both modes, a monochromatic x-ray beam (from synchrotron radiation) with varied wavelength (λ) is directed onto a sample, and the spectra of x-ray absorption are studied. In XANES, a narrow energy region located below the position of the absorption edge of the atoms of a given material is studied, and in EXAFS, a wider energy region located above this edge is investigated. X-ray absorption is usually determined either from the values of current caused by the x-ray induced electron emission or from the intensity of x-ray fluorescence.

XANES spectra provide information on the chemical state of a definite atom, in particular, about its oxidation state, effective charge, and immediate environment, while the analysis of EXAFS data allows one to investigate the positions of atoms located not only in the immediate vicinity of the atom of interest but also at greater distances, i.e., to determine the radial distribution functions.

F. X-ray photoelectron spectroscopy

This method is based on the phenomenon of external photoeffect—the emission of electrons under the impact of characteristic x-ray radiation. Thereby, the kinetic energy (E_{kin}) spectrum of the emitted electrons is recorded with an energy analyzer. For the ideal case of absolutely pure elementary substance, the value of E_{kin} is given by the relation

$$E_{kin} = h\nu - E_{bind} - \varphi, \quad (2)$$

where $h\nu$ is the energy of the incident photon, φ is the difference between the work functions of the investigated substance and the material of the first electrode of analyzer, and E_{bind} is the "binding energy" defined as the energy required to remove an electron from a certain energy level of an atom or from the valence band of a dielectric or semiconductor to an infinite distance. If the substance contains atoms of different chemical elements, i.e., for a chemical compound or a solid solution, the spectral position of the corresponding line in the photoelectron spectrum undergoes the so-called chemical shift, which makes it possible to determine the chemical composition of the material. The spectra contain large amount of information, the detailed consideration of which is beyond the scope of this article and is described in the specialized literature (e.g., Ref. 37).

Photoelectrons are emitted by atoms located not only directly on the surface but also at a certain depth. Usually, the thickness of the analyzed layer is 2–5 nm. If there are some contaminants on the surface or a natural oxide, they are removed by sputtering with a low-energy (∼ 1 keV) ion beam. Ion etching is used also to analyze the inhomogeneity of the chemical composition over depth.

When studying chemical compounds or solid solutions, the peaks in the x-ray photoelectron spectroscopy spectrum are often asymmetric, including the cases of overlapping of maxima corresponding to atoms of one and the same element in different chemical states. So, in β-Ga_2O_3, some gallium atoms are bonded to four neighboring oxygen atoms, while others are bonded to six (tetrahedral and octahedral Ga configurations, respectively) (Fig. 2). It is customary for oxides to use the term "oxidation state," meaning the number of oxygen atoms associated with a given one. To find the fraction of atoms in a particular oxidation state, the peak is decomposed into the functions that combine Gaussian and Lorentzian (deconvolution procedure). Interpretation of the resulting set of such functions is not always easy due to the ambiguity of the deconvolution procedure (this often requires some additional information or *ab initio* modeling). Another difficulty is that the asymmetric form of peak may be caused also by the inhomogeneity of phase composition in the analyzed layer. For example, in the case of Ga_2O_3, the phases of α-Ga_2O_3 and β-Ga_2O_3 may be present, as well as the inclusions of elemental gallium and nonstoichiometric oxides

G. Secondary ion mass spectrometry

This method is designed to reveal the chemical composition and incorporated species in the material studied. It allows measuring the distribution of impurity atoms over depth with a concentration sensitivity approaching 10^{13}–10^{14} cm^{-3}. Secondary ion mass spectrometry (SIMS) is based on the phenomenon of sputtering of solids by an ion beam. Although most of the sputtered atoms are electrically neutral, some of them are emitted in a charged state (secondary ions). With the help of electric and magnetic fields, these ions are separated according to their mass to charge ratio. In modern time-of-flight mass-analyzers, the separation is carried out according to their drift time in some space of the spectrometer.

Published under license by AVS.

The use of the focused probing ion beam in conjunction with the surface scanning makes it possible to determine the impurity concentration at different areas of the surface with a lateral resolution reaching 50–100 nm. To obtain depth concentration profiles, ion etching is performed either by the probe beam itself or with the help of a separate ion beam.

It should be noted that when using the SIMS technique, some difficulties are encountered, especially for high impurity concentration, when the sputtering coefficient may be concentration-depended, (e.g., see Ref. 38).

H. Scanning probe microscopy

Scanning probe microscopy (SPM) includes several methods or modes, the common feature of which is raster scanning of the sample surface with a sharpened probe, machine recording, and processing of the data. The advantage of SPM is its relative simplicity (unlike TEM, it does not require a complex procedure for the sample preparation), the large amount of information received, and very high maximal resolution. The two most commonly used SPM methods are atomic force microscopy (AFM) and scanning tunneling microscopy (STM).

AFM is most often used to study the surface morphology (although its capabilities are much higher). It is based on the fact that, at small distances, the force of interaction between atoms located on the surface of the sample and on the tip of the probe strongly depends on this distance. Precise movements of the probe (or sample) in the horizontal and vertical directions are carried out using piezomotors. The feedback arrangement, which includes a laser beam, a mirror fixed on the probe mount ("cantilever"), and a photodetector, ensures the maintenance of a given distance between the probe and the sample surface. With the use of an analog-to-digital converter and computer graphics, a 3D image of the relief is created. The typical resolution is of the order of a few nanometers.

STM is based on the phenomenon of electron tunneling through a potential barrier in the presence of a vacuum gap between the sample and the tip of the probe. At a given applied voltage between the sample and the probe, the value of tunneling current depends both on the local electrophysical properties of the sample surface and on the size of the vacuum gap. The feedback system uses the deviation of the tunneling current. In the surface relief mode, the system tracks and digitizes the vertical movement of the probe during scanning.

There is an additional mode of scanning tunneling spectroscopy (STS), which provides information on the local properties of the sample, such as the work function, the position of the Fermi level in the bandgap, I–V, and C–V characteristics. The values of spatial resolution in STS could be as high as of atomic scale, especially in ultrahigh vacuum. Such a high resolution is possible due to the exponential dependence of tunneling current on the size of the vacuum gap.

Scanning probe microscopy can be used (in combination with other methods) to study many processes during ion implantation: a change in conductivity of local areas due to the activation of implanted impurities, formation/annealing of disordered regions and defect clusters, synthesis of phase inclusions, etc.

I. Rutherford backscattering spectrometry with channeling

This method is based on measuring the energy spectrum of high-energy light ions (most often it is He^+ with $E \sim 1$ MeV), after Rutherford scattering from a crystalline sample. A well-collimated ion beam falls on the sample surface, and the yield of ions scattered at angles close to 180° is recorded.[39–41] Let us consider the Rutherford backscattering spectrometry with channeling (RBS/C) application in radiation damage under ion irradiation study. In this case, the energy spectra of unimplanted samples are measured first. (As a rule, crystals with a surface oriented perpendicular to the family of planes with low indices are used, since in this case the structural channels are wider, so the effect of ion channeling is better expressed.) The RBS spectrum is recorded with two orientations of the sample relative to the incident beam: with high misorientation (usually 7°) and with no misorientation ("random" and "channeling" spectra, respectively). In the first case, there is no channeling, and the spectrum coincides with the spectrum of the amorphous state. This spectrum has a steep drop on the high-energy edge. For a clean surface, this edge corresponds to the loss of ion energy due to the scattering from atoms located immediately on the surface. In the second case ("channeling" spectra), most of the incident ions move along the channels only with seldom scattering. In this case, the yield from ions that have not entered the channels, as well as those that left the channeling mode due to the nonideal structural perfection of the crystal, plus the yield from ions scattered from defects blocking the channels, are dominating in the spectrum of backscattered ions. For structurally perfect samples, the yield of ions backscattered in the near-surface region is very small. For the crystals having less structurally perfect layers, the channeling spectrum is characterized by the presence of a region with an increased value of the yield. The energy width of such regions is defined by the thickness of the layer with a damaged structure, and the yield value characterizes the degree of damage. Spectra processing using a special software[39–41] allows determination of the degree of damage as a function of depth. If an amorphous layer exists near the surface, then the yield of backscattered ions from it is equal to the yield of random spectra.

Thus, the RBS/C method allows studying the processes of accumulation and annealing of damage, including the process of solid-phase recrystallization of amorphous layers. In addition, the existence of isolated disordered regions (clusters) or extended defects that cause local stresses and, as a consequence, distortion of atomic rows forming the channel "walls," leads to increased yield from the layers located deeper than the implanted one. This allows revealing the presence of such objects.

In the case when implantation causes a transition of a substance to another crystalline phase (i.e., a polymorphic transformation), the most careful analysis of the RBS spectrum is required, since such a transformation can lead to a similar effect as that of accumulation of radiation defects or amorphization.

Another application of the RBS/C method is to study the concentration profiles of implanted impurities with atomic masses exceeding the atomic mass of the material studied. This is possible due to the fact that the energies of the ions scattered from such impurities lie in the region of higher energies in comparison with

Published under license by AVS.

the energy of the ions scattered from the intrinsic target's atoms, so that the corresponding peak in the RBS spectrum is separated by a certain gap from the main spectrum of substance. In addition to the determination of concentration profiles for such impurities, the RBS method makes it possible to determine the fraction of impurity atoms located on the lattice sites. Indeed, if an impurity atom is on a lattice site, this atom turns out to be screened by intrinsic lattice atoms located in the same atomic row, while atoms located in random positions or interstitial ones are not screened and give contribution to the yield of backscattered ions.

Thus, the RBS method provides important insights into the degree and kinetics of disordering, the lattice positions of heavy impurities and their distributions, as well as into the kinetics of damage annealing. However, the sensitivity of the method is limited to a few percent of the total concentration of atoms. In addition, this method, as a rule, does not provide direct information on the defect's types.

J. Electron beam induced current

The method is based on the generation of electron-hole (*e-h*) pairs in a semiconductor by an electron beam. The *e-h* pairs are separated in the space-charge region of a *p-n* junction or a Schottky barrier and induce a current. Electron beam scanning permits one to search a change of current over a surface. In particular, when the electron beam (in the SEM method) probes a region near the extended defect, the current is decreased due to an increased rate of *e-h* pairs recombination, and a respective contrast appears in the image. The same effect occurs in the cross-sectional mode of SEM. As it was demonstrated,[42] the EBIC also allows determining the diffusion length of minority charge carriers.

K. Deep level transient spectroscopy

Deep level transient spectroscopy (DLTS) allows determination of energy levels located in the semiconductor bandgap at large distances from the band edges.[43] The method is based on measuring the transient capacity of the Schottky barrier or *p-n* junction after the application of a voltage pulse providing nonequilibrium filling of deep energy levels by carriers. After the end of the pulse, the capacitance relaxes to its initial value due to the thermal ejection of the trapped charge carriers into the allowed band. The relaxation rate depends on temperature according to the Arrhenius law, which makes it possible to determine the spectrum of energy levels and their concentration by computer data processing.

One of the varieties of this method is the optical deep level transient spectroscopy, when filling of deep levels by carriers is performed not by electric but by optical pulse.[44,45]

Another variation of this method is the deep level optical spectroscopy (DLOS), which differs from the conventional DLTS method in that after filling the levels not the temperature but the energy of incident photons is changed.[20] DLOS has the following advantage over the conventional DLTS method: the levels can be determined across the entire bandgap, while the traditional DLTS is applicable to deep levels only.

L. PL and CL spectroscopy

PL spectroscopy is based on the analysis of photoluminescence spectrum arising from radiative electron transitions from higher to lower levels in the semiconductor bandgap, as well as from interband transitions. For PL excitation, usually monochromatic light sources (lasers) are used.

By using continuous spectrum light sources and a monochromator, the photoluminescence excitation (PLE) spectra can be measured, which provide information about the PL mechanisms. A pulsed excitation is used to determine the PL kinetics. It allows measuring the rate of nonradiative recombination associated with defects. Such information is important particularly to study the annealing processes of the damage accumulated under ion irradiation. The PL method is also used to determine the emission parameters of impurity centers.

In the method of cathodoluminescence spectroscopy, the excitation is carried out by irradiating the sample with electrons. This method is especially often used to study wide bandgap semiconductors, for which the PL spectroscopy requires the use of sources of hard ultraviolet (UV) radiation. An important advantage of CL spectroscopy is also the ability to estimate the depth (distance from the sample surface) at which the majority of certain luminescent centers are located. For this aim, the energy of incident electrons, and hence the thickness of the probed layer, is varied. When studying the samples subjected to ion implantation, this variation makes it possible to distinguish the contributions to luminescence of intrinsic impurities or defects, which are located uniformly (over all sample depths), and that of extrinsic ones introduced by ion implantation into the near-surface layer of the semiconductor only.

M. Electron paramagnetic resonance

For semiconductors, electron paramagnetic resonance (EPR) provides important information about the nature (configuration, elemental composition) of impurities and defects and their behavior when external conditions change, e.g., when irradiated samples are annealed. This method is based on the Zeeman effect—the splitting of energy levels of paramagnetic centers in a magnetic field. Paramagnetic centers contain unpaired electrons with spin. When a magnetic field with induction $\boldsymbol{B}$ is applied, the spin-degenerate energy levels are split. The difference ΔE of energy levels with and without a field is proportional to $\boldsymbol{B}$ and the coefficient of proportionality "g" is called the Lande factor g (g-factor). In a crystal, the electric fields of neighboring atoms (ions) surrounding a given impurity atom or defect affect the value of the g-factor. As the intracrystalline field is generally anisotropic, the g-factor is a tensor.

When measuring the EPR spectrum, in addition to the constant magnetic field, an ultrahigh-frequency electromagnetic field with a frequency $\boldsymbol{\nu}$ is applied to the sample. This field undergoes a resonance absorption when the value of its quantum $h\nu$ of energy coincides with the value of ΔE. (In real situations, the resonance is usually achieved by varying the magnetic field $\boldsymbol{B}$ at a fixed value of $\boldsymbol{\nu}$.)

Thus, by measuring the EPR spectrum and performing calculations in accordance with certain models, one can get insights into the structure of paramagnetic defect centers and their orientation with respect to the crystal axes. The paramagnetic defect centers

Published under license by AVS.

concentration is determined by using reference samples with a well-known number of centers.

N. Hall effect measurements

When current flows through the sample, the Lorentz force acts on the movement of charge carriers in a magnetic field, deflecting their trajectories and resulting in an additional electric field. This phenomenon is named the Hall effect, which, together with the measurement of electrical conductivity, is used to determine the type of conductivity, concentration, and mobility of charge carriers in semiconductors. In the case when the analyzed layer is located on an insulating substrate, the layer concentration of charge carriers n_s is determined from the relation connecting this parameter with the voltage between the measuring contacts, current, magnetic field, and geometry of contacts. The average value of charge carrier's mobility μ is determined from the relation $\sigma_s = q \cdot n_s\mu$, where σ_s is the layer conductivity and q is the charge of the electron. The type of conductivity can be found from the sign of the Hall voltage for a certain direction of the magnetic field. The ionization energies of impurities or defect centers are found from the temperature dependence of the charge carriers' concentration. To determine the depth distribution of specific conductivity and charge carrier's concentration, σ_s and n_s measurements should be provided together with step-by-step etching.

IV. PROPERTIES OF IMPLANTED Ga_2O_3 LAYERS

A. Properties of impurities in β-Ga_2O_3 introduced by ion implantation

Ion implantation is a well-established technique, widely used for the introduction of impurities and defects in solid materials since the early 1960s. In this technique, positive or negative ions extracted from solid or gaseous sources are accelerated through a potential difference and attain high kinetic energies. The accelerated ions usually pass through an electromagnet to select the desired kind of ions and are directed to the target (sample). Colliding with the atoms of the sample, the ions transfer part of their kinetic energy to them, displacing them from the lattice sites. Displaced atoms (recoils), acquiring sufficient kinetic energy, displace other atoms, and so on. Vacancies remain on the sites of displaced atoms. This process leads to the formation of radiation defects (discussed in more detail in Sec. IV B). When the implanted ion slows down to the energy at which it cannot produce recoils, it substitutes the vacancy becoming a substitutional atom, or stops at the nearest interstitial site becoming an interstitial atom.

This process enables introducing ions of any impurity ("ion" doping), including donors and acceptors, into semiconductors. However, due to the presence of radiation defects, the donor and acceptor properties of the introduced impurities usually appear only after annealing at sufficiently high temperatures, which eliminates defects or reduce their concentration. Annealing is carried out most often either in special furnaces for a long time from several minutes to several hours ("furnace annealing") or by lamp heating for several seconds ("rapid thermal annealing," RTA), less often—by other methods (current pulse, pulsed laser irradiation, etc.).

Nowadays, countless research groups around the world make regular use of this technique for modification of all sorts of materials, including semiconductors, metals, and insulators, in the form of bulk crystals, thin films, and nanostructures. Ion implantation is the key process of modern electronic technology.

The impurities introduced into β-Ga_2O_3 by ion implantation can be grouped into three main categories in accordance with the application of Ga_2O_3. *The first* category includes donor and acceptor impurities used to increase or decrease the majority charge carriers concentration—electrons: for creating Ohmic contacts, forming metal–oxide–semiconductor field-effect transistor (MOSFET) channels, producing high-resistance regions in order to reduce the edge leakage currents, and increase breakdown voltages. *The second* category includes impurities of rare earth elements and some transition metals used to create light-emitting centers. *The third* category includes light gaseous species—hydrogen (H), deuterium (D), and helium. Hydrogen impurity is used for the passivation of defect centers and also acts as a shallow donor. In addition, hydrogen and helium are used for the exfoliation of thin layers of Ga_2O_3.

The most often used impurities of *the first* category are the tetravalent elements of the fourth group of the periodic table—Si, Ge, and Sn. They replace the trivalent gallium atoms in gallium oxide and create shallow donor levels.

The electrical activation of Si implanted into an unintentionally doped (UID) float zone β-Ga_2O_3 crystals with surface orientation (010) was studied in Ref. 46. Using multiple-energy implantation of Si^+ with the maximum ion energy E of 175 keV, a 150 nm-deep doped layer was formed having a boxlike depth profile with Si concentrations in the range of 1×10^{19}–$1 \times 10^{20}\,cm^{-3}$. Postimplantation isochronous annealing was carried out in a nitrogen atmosphere at temperatures $T_{ann} = 700$–$1100\,°C$ with a step of 100 °C (30 min at each T_{ann}). Depth distributions of electron concentration were determined by electrochemical capacitance-voltage (ECV) measurements. The Si concentration profiles were also measured by the SIMS method. It was shown that, up to $T_{ann} = 1000\,°C$, the Si profiles are almost the same as in the as-implanted sample. At $T_{ann} = 1100\,°C$, the profile becomes nonmonotonous: near R_p (mean projected range of ions), there is a sharp increase in concentration, and in the region close to the surface, a similarly sharp decrease takes place. It is assumed that the Si redistribution is a consequence of the impurity diffusion to the region of maximum damage (i.e., segregation due to the interaction of impurities and defects).

Figure 4 shows the dependencies of estimated (by ECV measurements of $N_d - N_a$) concentrations of electrons in Si-implanted β-Ga_2O_3. The activation of the implanted impurity begins at 800 °C and reaches a maximum value at 1000 °C, decreasing with a further increase in T_{ann}, except for the case of the maximum Si dose, for which the dependence of electron concentration on T_{ann} is monotonous, but the fraction of activated impurity is very small (does not exceed 10%). The decrease in electrical activity of the impurity at high doses is apparently due to an increase in the fraction of Si atoms forming complexes with unannealed radiation defects (the concentration of the latter increases with the dose). The nonmonotonous behavior of the concentration of charge carriers with T_{ann} is possibly related to the outdiffusion of Si. However, the refinement of the mechanism of this impurity behavior requires further investigations.

Published under license by AVS.

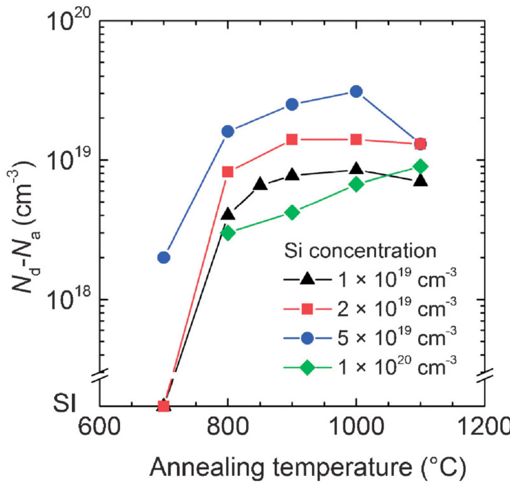

FIG. 4. Annealing temperature dependencies of electron concentration in the Si-implanted UID β-Ga_2O_3 layers. Reprinted with permission from Sasaki *et al.*, Appl. Phys. Express **6**, 086502 (2013) Copyright 2013, The Japan Society of Applied Physics.

The diffusion behavior of silicon implanted in β-Ga_2O_3 during RTA (T_{ann} = 1100 °C, annealing time of 10–120 s) was studied by the SIMS method.[47] As in Ref. 46, the Si boxlike profile was created by multienergy implantation (maximum ion energy E = 120 keV). Unlike Ref. 46, the surface orientation of the samples was (−201). It was found out that the annealing atmosphere had a significant effect on the Si diffusion: upon annealing in oxygen, the redistribution of impurities was much more pronounced than upon annealing in nitrogen. Moreover, in the case of oxygen annealing, there was a significant loss (outdiffusion) of silicon, which was not observed during annealing in nitrogen. According to the model proposed by the authors, this difference is due to the fact that annealing in nitrogen creates an increased concentration of gallium vacancies, which capture interstitial Si atoms and thereby slow down their diffusion.

In Ref. 48 of the same research group, the Si diffusion at 1150 °C was calculated on the basis of a simple (phenomenological) model that takes into account the concentration dependence of the diffusion coefficient. By comparing the experimental profile with the calculated one for different doses, the "low-concentration" diffusion coefficient at 1150 °C and the coefficient characterizing the concentration dependence of outdiffusion were determined. However, the use of only one T_{ann} for comparison and the phenomenological nature of the model do not allow judging on the applicability of the results obtained for other experimental conditions. In addition, the results may depend on the surface orientation due to the anisotropic structure of the monoclinic modification (β-phase) of Ga_2O_3.

Similar results were reported by this group for the implantation of two other (heavy) donor impurities of the fourth group—Ge^+ and Sn^+ (Refs. 48 and 49) and RTA with T_{ann} = 1100 °C. In the case of as-implanted samples, unlike the case of Si^+ ions, extended end-of-range defects were revealed by the cross-sectional TEM method. The authors discuss the difference in the diffusion mobility of Ge and Sn in terms of the difference in atomic radii, which is responsible for the local strains arising in the lattice around the substitutional atoms, and come to the conclusion that there is no correlation: the observed faster diffusion of Ge compared to Sn and Si cannot be explained by the difference of atomic radii of these impurities.

The diffusion behavior of implanted acceptor impurities like nitrogen and magnesium was studied by SIMS.[50] Mg^+ was implanted into a β-Ga_2O_3 (001) substrate doped with Sn at a concentration of 2×10^{18} cm^{-3}, and N^+ into a UID β-Ga_2O_3 (001) substrate with a charge carrier concentration of 2×10^{17} cm^{-3}. The maximum concentration of magnesium in the implanted samples was ∼10^{19} cm^{-3} and of nitrogen was ∼10^{18} cm^{-3}. The R_p values for Mg^+ and Si^+ ions were approximately the same (∼0.5 μm). Postimplantation annealing was carried out for 30 min at $T_{ann} \geq 600$ °C with a step of 100 °C in a nitrogen atmosphere.

It was found out that the redistribution of magnesium began at T_{ann} = 900 °C, while a significant redistribution of nitrogen occurred only at T_{ann} as high as 1100 °C. This circumstance is important, since it allows one, when using nitrogen ions, to increase the annealing temperature to higher values in order to provide more complete activation of the implanted impurity.

Interestingly, on the concentration profiles of Mg and N reported in Ref. 50, the regions exist where the concentration of these impurities practically coincides with the concentration of the impurity (silicon) in the initial samples. This indicates the formation of complexes consisting of the implanted and the original impurities due to donor-acceptor pairing: (Mg^-–Si^+), (Mg^-–Sn^+), and (N^-–Si^+). A similar phenomenon was observed for ion doping of Si and GaAs.[51–54] However, the effect of complex formation on the diffusion of impurities in β-Ga_2O_3 has not been studied. Thus, the physical nature of the difference in the diffusion behavior of Mg and N is not entirely clear. The difference may be due to the greater degree of radiation damage during the implantation of heavier ions (Mg), which was experimentally established in Ref. 50 using XRD. However, theoretical calculations performed by the DFT method[30] showed that even in the absence of implantation, the effective activation energy of Mg diffusion is lower than that for N. This may be explained[30] by the fact that nitrogen diffusion is dominantly assisted by oxygen vacancies, while magnesium diffusion is assisted by Ga interstitials.

In contrast to shallow donor impurities, acceptor impurities in β-Ga_2O_3 introduce deep levels into the bandgap.[23,29] Therefore, their activation during annealing and, accordingly, the compensation of donors leads to an increase in the resistivity, which was experimentally confirmed by *in situ* doping during the β-Ga_2O_3 growth process.[55,56]

In the case of ion implantation, defects such as gallium vacancies can also have a compensating effect.[10,15] In Ref. 57, nitrogen ions were implanted into epitaxial β-Ga_2O_3 layers with an initial electron concentration of 2×10^{18} cm^{-3}, and a boxlike profile of generated vacancies with a concentration of ∼ 10^{21} cm^{-3} was created. Measurements of the layer conductivity and the Hall effect of the N^+ irradiated samples demonstrate the formation of a semi-insulating layer, the resistivity of which remains practically unchanged up to T_{ann} = 600 °C. An increase in T_{ann} to 800 °C

Published under license by AVS.

causes the recovery of conductivity almost to its original level. This behavior indicates that the compensation of conductivity was caused not by the acceptor properties of nitrogen, but by the radiation defects. However, in Ref. 50, by measuring the leakage currents of the Schottky barrier, it was revealed that at $T_{ann} \geq 800\,°C$, the resistivity of the nitrogen-implanted layer increases with the annealing temperature.

In Ref. 58, the compensating effect of implanted nitrogen in β-Ga_2O_3 (with a silicon concentration of $3.9 \times 10^{17}\,cm^{-3}$) after annealing at 900 °C was established by measuring the *C–V* characteristics of the Schottky barrier. However, despite the fact that the concentration of implanted nitrogen was as high as $10^{20}\,cm^{-3}$, the electron concentration decreased as a result of N^+ implantation only to the level of $5 \times 10^{16}\,cm^{-3}$. This apparently was due to the low degree of nitrogen activation at such T_{ann} and indicates the need to use higher annealing temperatures. All these experiments prove that the mechanism of compensation by N^+ implantation depends on the nitrogen dose and annealing conditions.

In the case of Mg^+ implantation, the behavior of the leakage current with annealing temperature was nonmonotonous:[50] the leakage current increased in the range $600\,°C \leq T_{ann} \leq 900\,°C$ and decreased at $T_{ann} \geq 1000\,°C$. Note, that in this publication for magnesium and in Ref. 58 for nitrogen, the leakage current after annealing became higher than that before annealing (when the compensation was caused apparently not by the impurity Mg or N atoms, but by the radiation defects).

Let us now consider the implantation of impurities belonging to *the second* category, i.e., the rare earth elements Eu, Er, Gd, and transition metals. The behavior of these impurities was studied dominantly in connection with their luminescence properties.[59–63] Implantation was carried out into bulk β-Ga_2O_3 and nanowires of β-Ga_2O_3. For Eu^+ implanted into bulk β-Ga_2O_3,[60] the correlation between the implantation temperature, the temperature of postimplantation annealing, and the Eu concentration in the +3 charge state, on the one hand, and the cathodoluminescence spectra and intensity, on the other hand, were investigated. It was demonstrated that the radiation defects played a key role in the luminescence properties and charge state of Eu.

In Ref. 64, the features of Raman scattering spectra and CL of β-Ga_2O_3 nanowires and bulk crystals implanted with Cr^+ and Mn^+ ions with $E = 150\,keV$ and $D = 10^{15}\,cm^{-2}$ were studied. The measurement of Raman peaks linewidth showed that improving the structure during rapid thermal annealing of ion-irradiated nanowires began at 700 °C and finished at 1000 °C. The behavior of Cr-related cathodoluminescence at annealing was correlated with the structure improvement, and it was the same for nanowires and bulk samples, while in the case of Mn^+ implantation, the behavior in these objects was different. The physical reasons for the similarity or differences in the impurity's properties for implantation in bulk samples and in nano-objects are not yet clear.

Among light gas ions (belonging to *the third* category of implanted impurities), the most important is hydrogen.[3] It can penetrate as an unintended impurity during the growth of both films and bulk crystals. It is believed[3] that one of the main reasons for the commonly observed *n*-type conductivity in UID β-Ga_2O_3 may be the presence of residual hydrogen in the growth ambient. The donor properties of hydrogen were supported by theoretical calculations in the work.[17] It can also passivate deep acceptor impurity centers, reducing their efficiency.[25] However, it should be taken into account that hydrogen is a rapidly diffusing impurity and can escape from the semiconductor even at relatively low annealing temperatures (see below).

Interest with regard to the hydrogen impurity has been particularly increased after the exciting report in Ref. 65, where the authors claim that they have fabricated a low-resistive β-Ga_2O_3 of *p*-type by diffusion of this impurity.

To study the diffusion behavior of H, it is convenient to use its isotope D, because deuterium is easier to be detected than H. The relationship between the diffusion coefficients of H and D is defined by the relation $D_H/D_D = (M_D/M_H)^{1/2}$, where M is the mass of the corresponding atom.[66] The diffusion of deuterium introduced into β-Ga_2O_3 (−201) by ion implantation was studied in Refs. 67 and 68. Deuterium concentration profiles were measured by SIMS before annealing and after isochronous annealing (5 min each) at $T_{ann} = 450–650\,°C$. Comparison with the case of doping by plasma exposure (i.e., without ion implantation) allowed revealing the role of trapping hydrogen (or deuterium) by radiation defects (vacancies) in the diffusion mechanism. By comparing the experimental profiles with the calculated ones, the activation energies of various processes involved in H and D diffusion were determined.[68]

In Ref. 69, the structural and vibration properties of O-H centers in β-Ga_2O_3 were investigated by infrared polarized absorption spectroscopy. Hydrogen and deuterium were introduced into β-Ga_2O_3 (−201) samples by two ways: (a) by implantation and postannealing up to 400 °C; (b) without implantation—by annealing in H_2 and D_2 atmospheres. Infrared absorption spectra were measured at two different light polarizations. By comparing the spectra for the cases of doping with only hydrogen, only deuterium, as well as with hydrogen and deuterium together and using the results of DFT calculations, the authors of Ref. 69 concluded that the dominant O-H center in Ga_2O_3 hydrogenated by annealing in a hydrogen-containing atmosphere or by implantation was a relaxed V_{Ga}-2H complex. In Refs. 67 and 68, it was shown that hydrogen introduced in Ga_2O_3 without ion implantation undergoes outdiffusion at lower temperatures than the implanted hydrogen. This difference may be caused by trapping of hydrogen by the radiation defects generated by ion implantation.

The implantation of light gas impurities (H^+, He^+) was used for the exfoliation of thin Ga_2O_3 layers[70] (as it will be pointed below, this technique is needed to solve the problem of the low thermal conductivity of Ga_2O_3).

In Ref. 71, the formation of bubbles in β-Ga_2O_3 (010) upon implantation of He^+ ions with $E = 160\,keV$ and $D = 5 \times 10^{16}\,cm^{-2}$ followed by annealing at 200 °C and then at 500 °C was studied using XRD, TEM, and AFM. The growth of bubbles known as blistering and the formation of cracks were the main processes leading to the exfoliation of the implanted Ga_2O_3 layer.

Summarizing the existing knowledge concerning the physical aspects of ion doping of β-Ga_2O_3, it is obvious that this field is still at the initial stage of development. In particular, the role of radiation defects in the activation of implanted impurities during annealing should be more thoroughly studied. What is most important for practical application is to gain a deeper insight into the

Published under license by AVS.

TABLE II. Parameters characterizing the interaction of ions with β-Ga_2O_3 target. "Straggling" means a root-mean-square scatter of ranges. Range and straggling refer to the semi-infinite target; vacancies of Ga (V_{Ga}) and O (V_O) and their numbers in the 100 nm subsurface layer are indicated.

Ion type	Energy (MeV)	Range (μm)	Straggling (μm)	Numbers of vacancies in the 100 nm layer subsurface per ion	
				V_{Ga}	V_O
H	0.01	0.09	0.04	3	3
	0.1	0.59	0.09	<1	<1
	1	8.74	0.37	<1	<1
	10	3.34×10^2	8.06	<1	<1
	100	1.89×10^4	3.76×10^2	<1	<1
Ga	0.01	0.01	0.03×10^{-1}	8.03×10^1	9.10×10^1
	0.1	0.04	0.02	6.89×10^2	7.82×10^2
	1	0.39	0.12	6.06×10^2	6.83×10^2
	10	2.63	0.33	1.12×10^2	1.22×10^2
	100	9.62	0.42	1.64×10^1	1.71×10^1
Au	0.01	0.01	0.02×10^{-1}	8.27×10^1	9.38×10^1
	0.1	0.02	0.01	7.13×10^2	8.08×10^2
	1	0.13	0.04	2.99×10^3	3.36×10^3
	10	1.38	0.27	8.57×10^2	9.67×10^2
	100	8.44	0.66	1.76×10^2	1.93×10^2

properties of impurities introduced by ion implantation in Ga_2O_3 samples fabricated by different methods.

B. Ion-induced damage in Ga_2O_3

The generation of damage is one of the most important features of the ion implantation method. This can be used in many cases as a tool for material modification, while in other cases, the damage can have a detrimental impact on some of the material's properties.

When energetic ions penetrate through a substance, they transfer their energy to electrons and nuclei of the target. The type of ion-substance interaction depends on the ion energy and on the mass of the target atoms and impinging ions. The energy lost by the ions can be transferred to the nucleus [the so-called nuclear stopping power (S_n)], to the electrons [called electronic stopping power (S_e)], and to the phonons (thermal loss). When the energy transferred to the atomic nucleus by incident ion exceeds a certain *threshold* value (E_d), a recoil atom and a vacancy are formed. The energetic recoils in turn can produce additional recoils and vacancies, and so on. As a result, each incident ion creates one or more groups of point defects, consisting of interstitial atoms and vacancies. Such groups of defects are called "displacement cascades."

In Table II, the calculated parameters that characterize the interaction of three types of ions—H^+, Ga^+, and Au^+ ("light," "intermediate," and "heavy," respectively)—with different energies are presented as examples. Calculations were carried out using the SRIM code.[72]

The influence of mass and energy of ions on the type of ion trajectory and on the defect formation for the same examples is illustrated in Fig. 5.

Figure 5 clearly shows the drastic differences between the damage induced by irradiation with ions of different masses and energy. While the protons with the indicated energies penetrate through the subsurface layer (~100 nm thick) practically without producing recoil cascades and with very small nuclear energy loss (hence, with a negligible damage), the heavy ion (here it is Au^+) with typical energy $E \leq 1$ MeV produces large cascades near the surface. With an increase in the energy of heavy ions, the value of S_n decreases, while S_e increases, so the degree of damage in the ~100 nm subsurface layer decreases. [However, at very high energies (not shown in Fig. 5) of the so-called "*swift* ions," the role of electron losses becomes dominant in damage.) The behavior of ions with intermediate masses (e.g., Ga^+) is similar to the behavior of Au^+ ions with higher energy, as seen in Fig. 5.

Experimental investigations of damage in β-Ga_2O_3 under ion irradiation (excluding the case of swift ions) can be conditionally divided into three types. The investigations of the *first* type are devoted to the study of the damage degree and its distribution over depth, as well as to the study of the structure recovery caused by thermal postirradiation annealing. The main research method used in these works is RBS/C. The *second* type of investigations concerns mainly the point radiation defects—vacancies, intrinsic interstitials, and simple complexes. The main methods for identifying such defects are luminescence spectroscopy and DLTS (with their varieties). These methods make it possible to determine the energy levels of point defects and to compare them with the results of theoretical modeling. Such studies are possible mainly under the conditions of a sufficiently low degree of damage, which occurs typically for low doses of irradiation with relatively light ions.

In the studies of the *third* type, attention mainly is paid to the behavior of implanted impurities, while the damage is of interest mainly insofar as it affects the activation of implanted impurities.

Published under license by AVS.

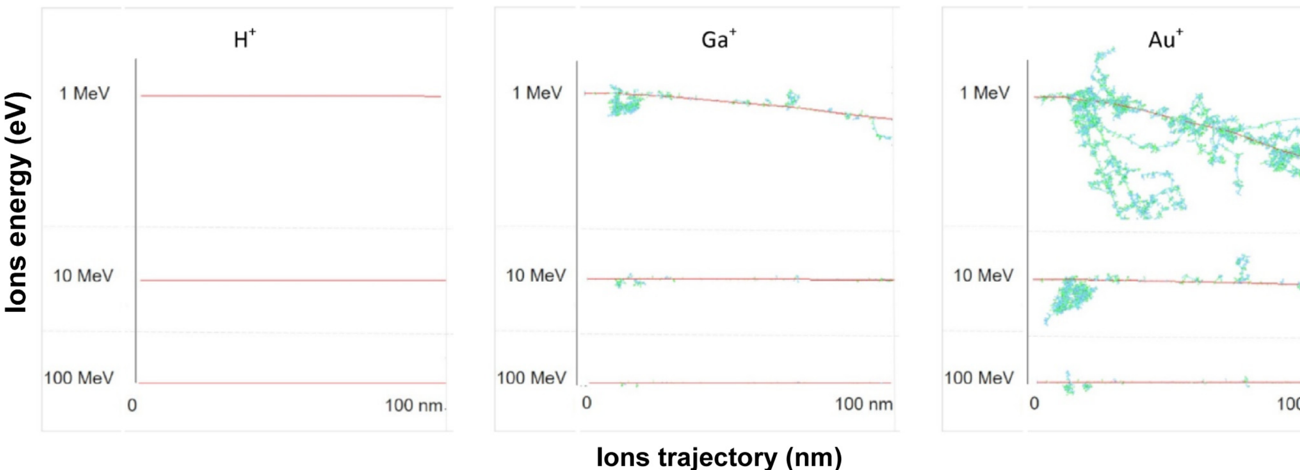

FIG. 5. SRIM simulations of damage induced in β-Ga_2O_3 by irradiation with H^+, Ga^+, and Au^+ ions at different energies. The ion trajectories are shown as continuous (red) lines while the Ga and O atoms displaced from their lattice positions (recoils) are shown as dots (green and blue, respectively).

These studies are considered in the Sec. IV A. The works devoted to irradiation by swift ions are considered, in brief, at the end of Sec. IV B.

Let us first examine the studies of the *first* type. In Ref. 73, the RBS/C method was used to study the dose dependence of the damage degree in β-Ga_2O_3 upon irradiation with P^+, Ar^+, and Sn^+ ions. Single-crystalline bulk β-Ga_2O_3 (010) was used. Energies (240–700 keV) were chosen so that the thickness of the implanted layer was the same for different ions—about 250 nm; the doses D were varied in the range of 1×10^{11}–2×10^{15} cm^{-2}. To minimize the channeling effect during implantation, the ion beam was 7° off axis. It was found out that the depth distributions of damage approximately corresponded to those calculated using the SRIM code.[72] In contrast to the behavior typical of semiconductors such as Si, Ge, and GaAs, the damage concentration did not reach 100% (the level of amorphization) with increasing dose, but reached a saturation value of ∼90% (see Fig. 6).

A similar behavior was previously observed in some other wide bandgap semiconductors with a high degree of ionicity, such as ZnO and GaN.[74,75] For β-Ga_2O_3, the degree of ionicity is lower than that of ZnO and GaN, and the saturation level is higher. In addition, for ZnO and GaN, the dose dependence of damage was characterized by the presence of two plateaus (intermediate and final), while for Ga_2O_3, the intermediate plateau was less pronounced and not in all cases (e.g., it was absent for Ar^+). The authors interpret the data obtained for the dose dependence of damage employing the model considered in Ref. 76. The latter is based on the assumption that upon ion irradiation, two types of primary defects are simultaneously generated: (a) elementary—single Frenkel pairs, which at each stage of irradiation partially recombine with defects generated at the previous stages, and (b) clusters. If the clusters are not amorphous, the model predicts the saturation of damage at a level less than 100%. The authors of Ref. 73 concluded that for a correct interpretation of the RBS/C data on the distribution of damage over depth, it is necessary to take into account also the bending of the channels due to the strains produced by defect clusters. It would be interesting to apply for the interpretation of the experimental results reported in Ref. 73 the models previously used in studies of damage under ion irradiation of other wide bandgap semiconductors, e.g., GaN and ZnO.[77–81]

The RBS/C method was also used in Ref. 59 to study the damage in β-Ga_2O_3 with (−201) surface orientation upon ion implantation of the rare earth element Eu (atomic mass $M = 152$). These results are somewhat different compared to Ref. 73. The difference, as noted in Ref. 73, is maybe due to two factors: a different surface orientation and a difference in the thickness of implanted layer. These factors are important when the surface serves as a drain for mobile defects. The energy of Eu^+ ion utilized was 300 keV, the doses (D) were 1×10^{13}, 1×10^{14}, 1×10^{15}, and 4×10^{15} cm^{-2}. The mean projected range R_p of Eu^+ was about 50 nm. It was found that, at the minimal dose used, the distribution of damage practically coincided with the vacancy distribution calculated using the SRIM code,[72] but it differs significantly at higher doses (illustrated in Fig. 7). For $D = 1 \times 10^{14}$ cm^{-2}, the damage decreases monotonically with depth and, for $D = 1 \times 10^{15}$ cm^{-2}, the distribution acquires a two-peak shape: the first peak is adjacent to the surface, and the second one (bulk peak) is located at a depth exceeding R_p. Moreover, in the area of the first peak, in contrast to the data,[73] the degree of damage reaches the amorphization level. With a further increase in the dose to 4×10^{15} cm^{-2}, the near-surface peak expands, then it merges with the bulk one, and the total layer thickness with the level of damage corresponding to amorphization reaches a value close to R_p.

These regularities are similar to those observed in the case of irradiation of GaN with heavy ions:[79,80] a two-peak distribution of damage and an increase in the thickness of the near-surface amorphized layer with increasing dose were also observed. The authors of Refs. 79 and 80 attribute the presence of the near-surface

Published under license by AVS.

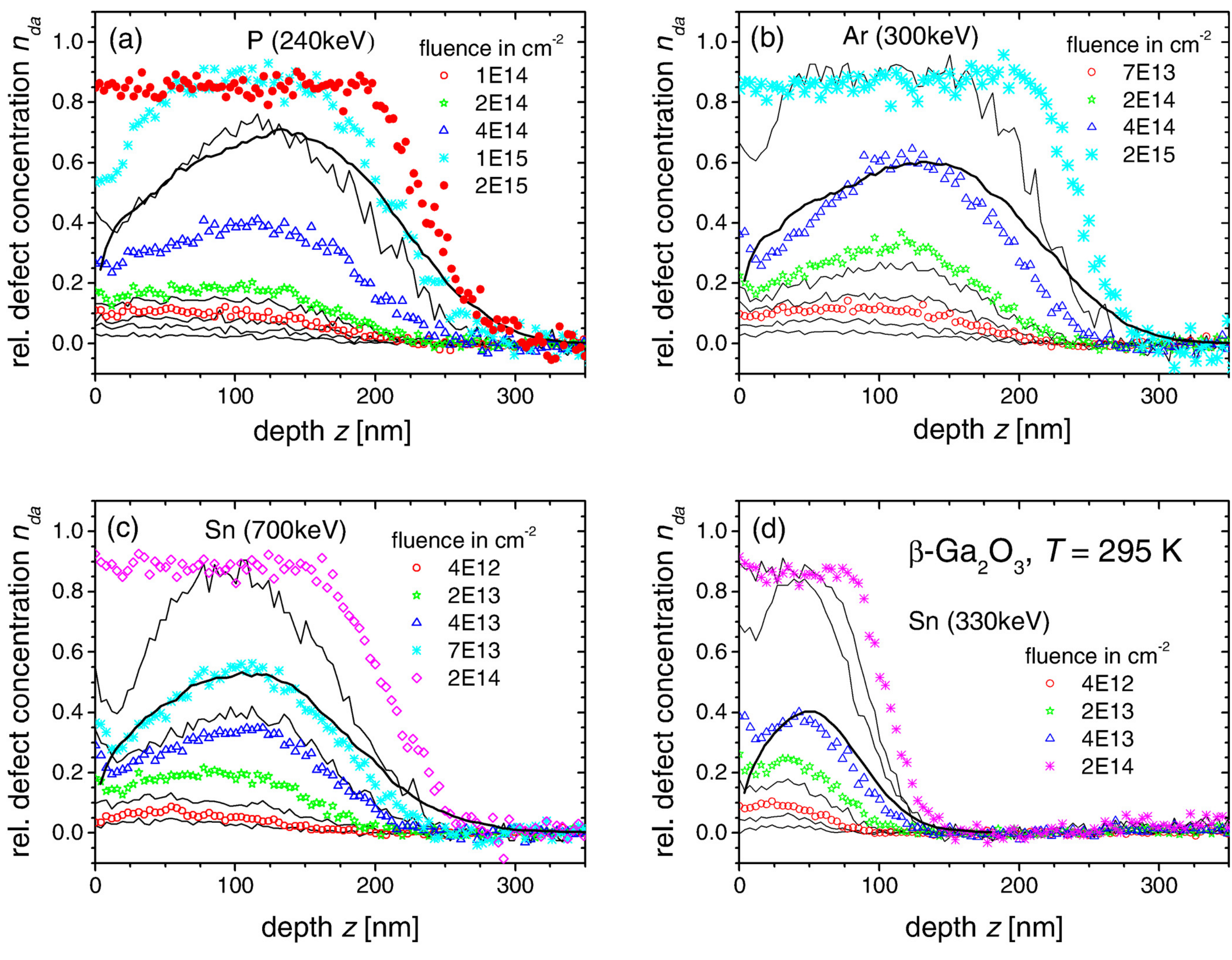

FIG. 6. Relative damage level n_{da} vs depth z for β-Ga_2O_3 implanted at room temperature with (a) 240 keV P, (b) 300 keV Ar, (c) 700 keV Sn, and (d) 330 keV Sn ions. For clarity, only selected ion fluences are indicated. The thick solid line is the depth distribution of primary displacements as calculated by SRIM given in arbitrary units for comparison. Reprinted with permission from Wendler *et al*., Nucl. Instrum., Methods Phys. Res., Sect. B **379**, 85 (2016). Copyright 2016, Elsevier.

peak to the diffusion of mobile point defects from the bulk peak to the surface or to the boundary of the amorphous region (after amorphization near the surface). This explanation later supported by Ref. 60 may apparently be valid also for β-Ga_2O_3. As noted in Refs. 79 and 80, the presence of two damage maxima in the case of GaN is typical of heavy ions (the Eu^+ used in Ref. 59 also corresponds to the type of heavy ions). Possibly, in the case of GaN and β-Ga_2O_3 (−201), the drift of point defects in the field of elastic stresses plays a role: the latter grows with increasing ion mass.

Interestingly, as seen in Fig. 7, the tendency to saturation of damage is noticeable at certain depth. Another interesting feature observed in Ref. 59 is the nonmonotonic dose dependence of RBS/C yield for high depths (deeper than the implanted layer). The RBS/C level at these depths is significantly lower at doses at which amorphization occurs. The authors of Ref. 59 explain this by the fact that, while extended defects appear at comparatively low doses, causing dechanneling of He^+ ions, such defects are absent upon amorphization.

The study of annealing effect on the distribution of damage in β-Ga_2O_3 implanted by Eu^+ ions ($4 \times 10^{15}\,cm^{-2}$)[59] also revealed a number of interesting features. RTA was carried out in an argon flow within the temperature range $T_{ann} = 500$–1200 °C. After annealing at 500 °C, there is a slight decrease of damage at all depths (except for the tail section, where the occurrence of extended defects is assumed). A more significant recovery of the crystalline quality occurs at $T_{ann} = 700$ °C and $T_{ann} = 900$ °C when the distribution of damage has a two-peak character. Apparently, at such temperatures, a fraction of defect complexes decomposes into

Published under license by AVS.

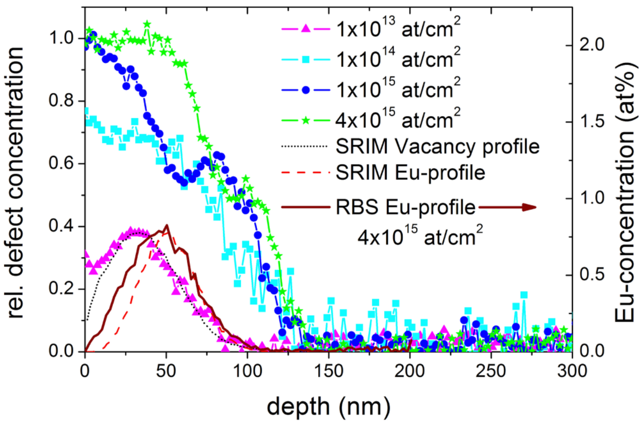

FIG. 7. Relative defect concentration as a function of depth for Ga_2O_3 implanted by Eu^+ to different fluences. The profiles of defects and Eu atoms calculated using the SRIM code are also shown (in arbitrary units) as well as the Eu-profile extracted from the RBS spectra of the sample implanted with $D = 4 \times 10^{15}\,cm^{-2}$. Reprinted with permission from Lorenz *et al.*, Proc. SPIE **8987**, 89870M (2014) Copyright 2014, Society of Photo-Optical Instrumentation Engineers (SPIE).

simpler mobile defects, which diffuse to the surface, while other fraction interacts with the Eu atoms and forms impurity-defect complexes. It can be noted that, at T_{ann} = 700–1000 °C, the damage increases with temperature at the depths where the maximum concentration of Eu is located. This is consistent with the authors' assumption that the defects and Eu impurity stabilize each other. Finally, at T_{ann} = 1100 °C, an almost complete recovery of the crystalline quality of β-Ga_2O_3 takes place, and this is accompanied by a redistribution of Eu atoms—they move toward the surface.

In Ref. 60, the RBS/C method was used to study the effect of temperature during the implantation (T_{imp}) on the crystalline quality of β-Ga_2O_3 (−201), as well as the impact of postimplantation annealing after "hot" implantation by Eu^+ ($E = 300$ keV, $D = 1 \times 10^{15}\,cm^{-2}$). It is demonstrated that the crystalline quality nonmonotonically depends on T_{imp} and T_{ann}. At T_{imp} = 400 °C and T_{imp} = 600 °C, the quality is significantly higher than that at T_{imp} = 20 °C, while it decreases with elevation of T_{imp} to 800 °C and increases again only at T_{imp} = 1000 °C. A similar dependence was observed for the annealing of samples irradiated at T_{imp} = 300 °C and T_{imp} = 600 °C in the range of T_{ann} = 700–1000 °C. In this case, as the T_{ann} increases, the fraction of Eu atoms replacing the lattice sites decreases. This behavior additionally confirms the conclusions of Ref. 59, according to which defects and impurities mutually stabilize each other. Apparently, the interaction between them may be enhanced by local elastic stresses around impurity atoms. As in Ref. 73, the RBS/C data presented in Ref. 60 indicate the existence of extended defects.

The TEM and SEM methods were applied in Ref. 82 to investigate thermally evaporated Ga_2O_3 nanowires irradiated with Eu^{3+} and Gd^{3+} ions. It is found by SEM that nanowires have a complex shape and are oriented randomly in projection onto the substrate plane. The presence of an amorphous phase after irradiation is proven by TEM. A correlation between the structural changes (revealed by TEM) and CL is established. The recovery of crystalline quality upon annealing was investigated by Raman spectroscopy, which demonstrated the recovery started at T_{ann} = 500 °C and finished at 1100 °C. Study on β-Ga_2O_3 nanowires irradiated with Eu^+, Gd^+, and ions of some transition metals was performed in Refs. 62, 63, and 83, where similar results were reported.

In Ref. 84, a detailed electron microscopy examination of epitaxial β-Ga_2O_3 layer irradiated by Ge^+ ions with doses and energies of $3 \times 10^{13}\,cm^{-2}$/60 keV, $5 \times 10^{13}\,cm^{-2}$/100 keV, and $7 \times 10^{13}\,cm^{-2}$/200 keV was performed. It is found out that the damaged layer undergoes a phase transition from the β-phase to the κ-phase during irradiation. Postimplantation annealing at 1150 °C for 60 s in an O_2 atmosphere leads to the reverse transformation of κ-phase into β-phase, except for a thin layer (∼ 17 nm), which keeps the structure of the k-phase. In addition, a change of oxygen environment extended deeper than the implanted zone was discovered. These results show that the conclusions about damage accumulation and amorphization, which are based on RBS/C data, should be proven by direct structural methods, such as electron microscopy or XRD. In addition, they show the need for a thorough study of the starting material and the irradiation conditions influences, as well as the conditions of postimplantation annealing, on the nature of damage and structural-phase transformations under ion irradiation using various methods of analysis.

Let us now consider the investigations of *the second* type, where the point defects generated by ion irradiation are considered. In Ref. 85, the samples of β-Ga_2O_3 were irradiated by O^+ ions with $E = 25$ MeV and $D = 1.5 \times 10^{11}$, 5×10^{11} and $1.5 \times 10^{12}\,cm^{-2}$. The main information was obtained by PL spectroscopy. It is established that the PL spectra of irradiated samples are similar to the spectra of nonirradiated ones; however, the emission intensity is significantly higher. With increasing dose, the PL intensity decreases, apparently due to the accumulation of defects serving as the centers of nonradiative recombination. Considering the PL spectroscopy data, as well as the results of *ab initio* calculations,[86] the authors identified the deconvoluted PL peaks with divacancies ($V_{Ga} + V_O$), gallium vacancies (V_{Ga}), and interstitial oxygen atoms (O_i). The PL in this work was excited at a photon energy of 3.8 eV, which is lower than the bandgap of β-Ga_2O_3. The peak at 3.8 eV was found in the PLE spectrum.

In Ref. 87, β-Ga_2O_3 layers with an initial electron concentration of $4.8 \times 10^{17}\,cm^{-3}$ grown on an MgO substrate were irradiated at 35 K by C^+ ions with $E = 1.5$ MeV and various doses up to $10^{14}\,cm^{-2}$. The resistivity of films increased by more than 8 orders of magnitude, which was explained by the generation of defects that introduced deep levels into the bandgap. The quantitative interpretation of the results was carried out on the basis of charge neutrality level theory[88] (see also Refs. 89–91).

The formation of defects under high-energy irradiation with light ions was studied in Refs. 92 and 93. Epitaxial β-Ga_2O_3 (010) layers with an Si concentration of $\sim 10^{16}\,cm^{-2}$ were irradiated with protons with $E = 10$ and $E = 20$ MeV at $D \approx 10^{14}\,cm^{-2}$. The samples were characterized by the C–V method, C–V profiling under illumination, photocapacitance, DLTS with electrical and optical excitations, as well as by DLOS. It is found that irradiation introduces

Published under license by AVS.

several deep levels (traps) located both in the upper half of the bandgap ($E_c - 0.6$ eV, $E_c - 0.75$ eV, $E_c - 1.05$ eV, $E_c - 2.16$ eV) and in its lower half ($E_v + 0.2$ eV, $E_v + 0.4$ eV, $E_v + 1.3$ eV). The level ($E_v + 1.3$ eV) is attributed to gallium vacancies, while the levels ($E_c - 1.2$ eV) and ($E_c - 2.3$ eV) are close to the charge transfer levels of two types of oxygen vacancies predicted by the first-principle calculation in Ref. 17. The authors associate the level ($E_v + 0.2$ eV) with the STH state. (After being trapped at the STH level the hole should become immobile.) According to DFT calculations,[16] the transition of a hole from the valence band to the STH level and thus their immobilization is an energetically favorable process. This is one of the main factors making it difficult to obtain *p*-type β-Ga_2O_3.[3] However, the authors of Refs. 42, 92, and 93 come to the conclusion that holes generated by light or by electron beam may be mobile. The conclusion about the existence of β-Ga_2O_3 with mobile holes, i.e., having *p*-type conductivity, was also made in Refs. 94, and 95. Note, however, that the conclusion concerning the *excited* holes cannot be automatically transferred to the case of an *equilibrium* state of β-Ga_2O_3 doped with acceptor impurities.

In Ref. 21 single crystals and epitaxial layers of β-Ga_2O_3 were irradiated with protons at $E = 0.6$ and $E = 1.9$ MeV and $D = 5 \times 10^9$–6×10^{13} cm^{-2}. The irradiated samples with Schottky barrier were studied by DLTS and *C*–*V* methods, as well as by measuring the capacity recovery during heating. To interpret the obtained results, a series of *ab initio* calculations of the energy levels of various types of elementary point defects and complexes were performed. Some of the complexes considered contain hydrogen. In addition, the barriers for defect migration and recombination (trapping) were calculated. It was argued that the identification of experimental data of electron transitions requires taking into account all these factors, as well as shift of Fermi level and its pinning. Therefore, not only statistics but also defect kinetics and temperature factors are important. The conclusion was made that the compensation of electronic conductivity under proton irradiation could be explained by the presence of Ga interstitials, gallium vacancies, and Ga_O antisites, and that the migration and subsequent passivation of V_{Ga} with hydrogen might be responsible for the thermal recovery process.

Electrical and optical methods provide information on the energy levels, but they do not give the answer on the nature of defects. More informative for paramagnetic point defects is the method of EPR, used in Ref. 34. The UID β-Ga_2O_3 samples with a carrier concentration of 2×10^{17} cm^{-3} and semi-insulating β-Ga_2O_3 samples doped with Fe were irradiated by protons at $E = 12$ MeV and $D = 10^{16}$ cm^{-2}. It is concluded that the assumption about the presence of single gallium vacancies in the irradiated samples is inconsistent with experimental data and that more probable is the V_{Ga}-Ga_i-V_{Ga} complex predicted in Ref. 15.

A special type of damage is generated during irradiation by *swift* heavy ions, when the formation of ion tracks occurs. The tracks can be considered as cylindrical straight regions around the ion path when the energy S_e deposited by the ion exceeds the value required for melting of the material. The rapid quenching freezes the defects resulting in the formation of cylindrical regions with significantly changed atomic density and structure.[96–98] For some materials, the ion tracks may be amorphous,[99] while for others, the swift ion irradiation induces the recrystallization of an amorphous matrix[100] or forms the crystalline tracks with a different density and structure compared to the surrounding matrix.

The irradiation of β-Ga_2O_3 by swift ions was investigated also in Refs. 101 and 102. In Ref. 101, the case of irradiation by Au^+ at $E = 946$ MeV and D up to 1×10^{13} cm^{-2} was considered. Using XRD, the amorphous structure of tracks was established. Their diameter was estimated to be 8.3 nm using the model of "inelastic thermal spike" (i-TS).[103–105] In Ref. 102, TEM was utilized to study the tracks formed in β-Ga_2O_3 (100) under irradiation by swift ions of ^{86}Kr and ^{181}Ta. The authors confirmed the amorphous structure of the tracks and found that with an increase in electron losses S_e from 18.3 to 41.8 keV/nm, the average track diameter increased from 2.2 to 8.8 nm. The data on the track diameters and the threshold value of S_e for the track formation were in good agreement with the i-TS model.

V. Ga_2O_3-BASED DEVICES

A. Power electronic devices: MOSFET and SBD

The need to improve the efficiency of communication systems and some types of electrical equipment, such as inductive motor controllers and power supplies, requires the development of power electronics components with the parameters unattainable for previously used semiconductors. As a base material for such devices, β-Ga_2O_3 is of particular interest[3,7] due to its large bandgap, which provides a high breakdown voltage V_{br}, the ability to withstand high temperatures, as well as the possibility to change the conductivity over a very wide range by doping. When choosing a material for the power devices fabrication, a very important criterion is the Baliga figure of merit (BFOM),[106] which determines the power losses during device operation: the higher the BFOM is, the lower power losses are. The relation $\mathrm{BFOM} = V_{br}^2/R_{on}$ is based on the assumption that power losses are due to energy dissipation in the "on-state" resistance R_{on}. (It should be noted that BFOM can be used for devices operating at low frequencies or at direct current.[106])

Ion implantation of β-Ga_2O_3 was investigated for the development of two types of power devices—MOSFET and Schottky barrier diode (SBD). In particular, the implantation of Si^+ ions into β-Ga_2O_3 layers was used to form ohmic contacts for SBD,[46,50,107] contact regions of the source/drain, and the channels of MOSFET.[108–117] By Mg^+ or N^+ implantation into β-Ga_2O_3 layers, a current blocking layer (CBL) in vertical-type MOSFET devices was created,[113–115] as well as high-resistance regions and guard rings (GR) near the SBD anode.[107,118] In Ref. 119, the possibility to create both low-resistance regions for the formation of ohmic contacts and high-resistance layers near the edges of the SBD anode by Ar^+ implantation was shown. For the formation of MOSFETs on heterogeneous structures, a method of exfoliation and bonding was developed, based on irradiation with H^+ and Ar^+.[120,121] Let us consider these works in more detail.

From the analysis of data reported,[46,50,107,108,110,112–115] it is possible to trace the evolution of the purposes for which the ion implantation was used over the past few years. In the early work of this group,[46] the electrical properties of β-Ga_2O_3 layers upon implantation of Si^+ ions followed by annealing were investigated,

Published under license by AVS.

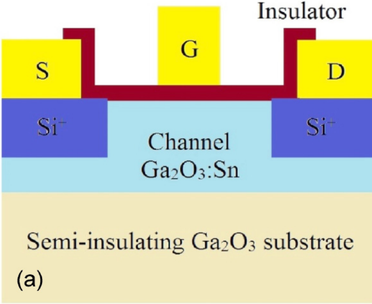

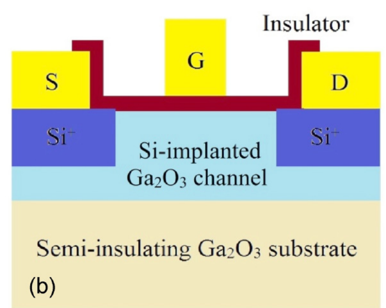

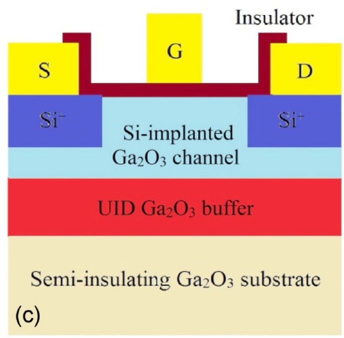

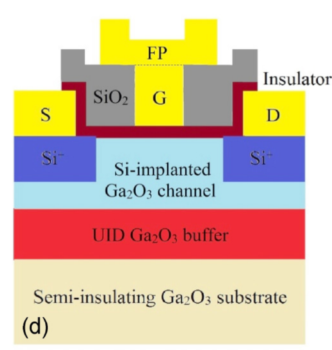

FIG. 8. D-mode MOSFET designs with regions created by Si^+ implantation: (a) with n^{++} near-contact source/drain regions; (b) the same as (a), but with a channel formed by Si^+ ion implantation; (c) the same as (b), but with an additional buffer layer; (d) the same as (c), but with an additional FP electrode.

and the possibility of creating ohmic contacts by Si^+ implantation into the near-contact regions of devices was for the first time shown [Fig. 8(a)]. Multiple Si^+ ion implantation was performed at energies $E = 10–175$ keV. The total implantation dose D varied from 2×10^{14} to $2 \times 10^{15}\,cm^{-2}$. The activation annealing was carried out at temperatures of 900–1000 °C in an N_2 atmosphere for 30 min. Ti (50 nm)/Au (300 nm) layers were used as ohmic contacts. At the concentration of implanted Si of $5 \times 10^{19}\,cm^{-3}$, the authors achieved the specific contact resistance $\rho_c = 4.6 \times 10^{-6}\,\Omega\,cm^2$, which was an order of magnitude lower than in the case of Sn diffusion[122] and lower than in Refs. 124 and 124. In Refs. 124 and 124, Si^+ implantation was provided at $E = 30$ keV and $D = 1 \times 10^{15}\,cm^{-2}$, activation annealing was carried out at a temperature of 950 °C, and ohmic contacts were created by the deposition of indium tin oxide or aluminum zinc oxide films with subsequent deposition of a Ti/Au film (the values of ρ_c were 6.3×10^{-5} and $2.8 \times 10^{-5}\,\Omega\,cm^2$, respectively).

In subsequent works,[108–110,112] ion implantation was used in the development of a depleted-mode MOSFET (D-mode MOSFET). At the initial stage, Si^+ implantation was used only for the formation of ohmic n^{++} contact regions to the source/drain,[108] while the channel was created by Sn doping during the growth of Ga_2O_3 film. Si^+ ions were implanted to a depth of 150 nm. The Si concentration in the implanted regions was $5 \times 10^{19}\,cm^{-3}$. The activation annealing was carried out at a temperature of 925 °C in an N_2 atmosphere for 30 min. The ρ_c value was $8.1 \times 10^{-6}\,\Omega\,cm^2$. Since the Si concentration near the surface was lower than in the region of the distribution maximum (due to the Gaussian profile of the impurity during ion implantation), a 13-nm-deep recess in the source and drain regions was made before metallization by reactive ion etching. The Ti(20 nm)/Au(230 nm) films were used as contacts. In this way, devices were created with the following characteristics: a gate length $L_g = 2\,\mu m$; drain current $I_d = 39$ mA/mm at gate voltage $V_g = +4$ V; breakdown voltage $V_{br} = 404$ V at $V_g = -20$ V; the ratio of currents in open and closed states $I_{don}/I_{doff} > 10^{10}$. The MOSFET characteristics remain stable over the operating temperature range (20–250 °C).

In continuation of this series of works, Si^+ implantation was used not only to improve the ohmic contacts but also to form the MOSFET channels. For this purpose, a 300-nm-deep n-type region was created by implantation of Si^+ into a β-Ga_2O_3 film grown by molecular beam epitaxy on a semi-insulating gallium oxide substrate [exhibited in Fig. 8(b)].[109] Implantation conditions during the channel formation[109,110] were $E = 10–330$ keV and $D = 1.1 \times 10^{13}\,cm^{-2}$. Annealing was carried out under the conditions specified in Ref. 108. The average concentration of charge carriers in the channel was $3 \times 10^{17}\,cm^{-3}$. The authors also noticed the advantage of the channels formation by Si^+ implantation as compared to Sn doping during the epitaxy of a Ga_2O_3 layer when the Sn impurity segregation took place.[112] The creation of a channel by Si^+ ion implantation made it possible to improve the characteristics of the MOSFET in comparison with Ref. 108 and to obtain a MOSFET with the following parameters: $I_d = 65$ mA/mm at $V_g = +6$ V; $V_{br} = 415$ V at $V_g = -30$ V; $I_{don}/I_{doff} > 10^{10}$.

In Refs. 108 and 109, a β-Ga_2O_3 wafer with a Fe concentration of $\sim 10^{18}\,cm^{-3}$ was used as a semi-insulating substrate. However, subsequent studies[110] showed that in this case there was an enhanced diffusion of Fe atoms from the semi-insulating substrate into the implanted semiconductor layer due to defects formed upon Si^+ implantation. This diffusion leads to deterioration in the

Published under license by AVS.

MOSFET performance. However, the formation of a buffer UID β-Ga_2O_3 layer between a semi-insulating substrate and an Si^+ implanted channel [Fig. 8(c)] effectively eliminates the penetration of Fe into the channel region.[110]

In Ref. 111, an additional field-plate (FP) electrode [FP-MOSFET mode, Fig. 8(d)] was introduced into the device design, which made it possible to achieve the following device parameters: $V_{br} = 755$ V at $V_g = -55$ V; $I_d = 78$ mA/mm at $V_g = +4$ V. It should be noted[111] that there was practically no variation of the drain current with the stability of characteristics up to operating temperatures of 300 °C.

So far, D-mode MOSFETs were discussed. However, the enhanced-mode (E-mode) MOSFETs are widely used in digital and power electronics. In Ref. 126, Si^+ implantation was used for the development of devices with n^{++} contact regions of the source/drain (Fig. 9). The devices were characterized by a low parasitic resistance between the source and drain (2.2 Ω mm) and a small specific contact resistivity ($\rho_c = 7.5 \times 10^{-6}\ \Omega\ cm^2$).

Even better characteristics of MOSFETs with n^{++} source and drain contact regions formed by Si^+ implantation were achieved in Refs. 116, 117, and 126, where a higher implantation dose ($1.5 \times 10^{15}\ cm^{-2}$) was used. Ion energies during multiple implantations were 10, 30, 60, and 100 keV. The total implantation depth was 210 nm, and the average silicon concentration was $10^{20}\ cm^{-3}$. For the D-mode FP-MOSFET, the following parameters were achieved: $V_{br} = 720$ V, when the devices operated in air, and $V_{br} = 2360$ V, when operated in a mixture of inert gas with fluorine. In Ref. 127, the values of $V_{br} = 2900$ V and BFOM = 182 MW cm^{-2} were obtained for devices of this type (at the distance between the gate and drain $L_{GD} = 17.8\ \mu m$) using a T-shaped gate and Al_2O_3/HfO_2 layers as a gate dielectric. For the E-mode FP-MOSFET,[127] the use of Si^+ implantation for the source and drain formation made it possible to achieve the following values of V_{br}, BFOM, and contact resistance R_c: 3000 V, 94 MW cm^{-2}, and 2 Ω mm, respectively. Finally, in Ref. 129, Si^+ implantation was used to form a source and drain, a self-aligned gate (SAG), and a thin channel (22 nm). A record value of the maximum transconductance of 35 mS/mm was obtained. The R_c value was 1.5 Ω mm.

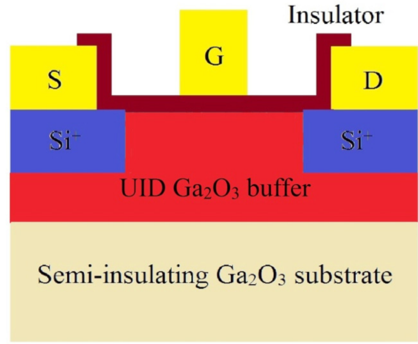

FIG. 9. E-mode MOSFET design with n^{++} ion-implanted source/drain contact regions.

The β-Ga_2O_3 disadvantage is its very low thermal conductivity, which creates certain problems in the development of power electronic devices based on this material. To improve the conditions for heat dissipation, it seems that it would be sufficient to deposit thin films of gallium oxide on materials with a higher thermal conductivity, e.g., on Si or SiC.[120,121] However, due to the large lattice mismatch, the synthesis of β-Ga_2O_3 films with high-quality on such substrates is problematic. In Refs. 119–121, the ion-cutting (exfoliation) technique was used to eliminate this disadvantage. Bulk β-Ga_2O_3 was implanted with high-dose H^+. After that, an interface layer was formed on the wafer surface by deposition of Al_2O_3 or amorphization of β-Ga_2O_3 by irradiation with Ar^+ ions, and the resulting structure was bonded with an Si or SiC substrate. During the subsequent annealing, the implanted hydrogen migrated and accumulated at a certain depth, creating a high level of stress. As a result of this stress, the exfoliation of β-Ga_2O_3 thin layer occurred. Since the conductivity of Ga_2O_3 film was deteriorated upon H^+ implantation, the obtained heterogeneous structure was doped by Si^+ implantation at $E = 15$ keV and $D = 5 \times 10^{13}\ cm^{-2}$, after which D-mode and E-mode MOSFETs were fabricated on the gallium oxide film. The source and drain areas were doped using additional silicon implantation. The authors noted the high stability of the obtained devices characteristics in comparison with the devices fabricated on β-Ga_2O_3 substrates. The breakdown voltage V_{br} was 570 V at 300 K and increased to 605 V at 500 K.

Now, let us consider the use of Mg^+ and N^+ acceptor impurities implantation for the development of power electronic devices. In Ref. 50, the effect of Mg^+ and N^+ implantation as well as the subsequent activation annealing temperature was investigated in order to establish which of the conditions were more efficient for the development of high-voltage SBDs. The conditions for Mg^+ implantation into β-Ga_2O_3 (grown by the EFG method) were the following: $E = 560$ keV and $D = 6 \times 10^{14}\ cm^{-2}$. The magnesium concentration at a depth of 0.5–0.6 μm was $1.5 \times 10^{19}\ cm^{-3}$. Subsequent annealing was carried out at temperatures of 600–1000 °C for 30 min in an N_2 atmosphere. N^+ implantation was carried out into UID β-Ga_2O_3 at $E = 480$ keV and $D = 4 \times 10^{13}\ cm^{-2}$. The nitrogen concentration at a depth of 0.5–0.6 μm was $1.5 \times 10^{18}\ cm^{-3}$, and postimplantation annealing was performed at 800–1200 °C. Due to the insufficiently high concentration of charge carriers in the UID β-Ga_2O_3 substrate, ohmic contacts were formed using Si^+ implantation. It is found that, in contrast to the layers with N^+ implantation, defect clusters are formed in β-Ga_2O_3 layers implanted by Mg^+. As a result, with an increase in annealing temperature, the leakage current increases. For the samples with N^+ implantation, the leakage current, on the contrary, decreases. Therefore, using N^+ ions gives better results.

In Refs. 113–115, the results of Ref. 50 are used to design a vertical mode MOSFET (Fig. 10), in which the gate and source are located on one side of the crystal, and the drain is formed on the opposite side. It is noted[113] that for high-voltage and high-power devices, vertical mode is highly desirable since it allows superior field termination and current drives. For such MOSFETs, it becomes necessary to form areas of charge carrier drift by creating a CBL. This layer was formed by Mg^+ and N^+ ion implantation into gallium oxide layers grown by the halid vapour phase epitaxy (HVPE)

Published under license by AVS.

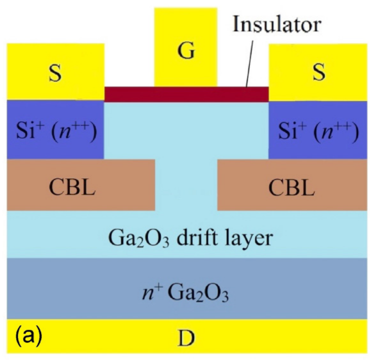

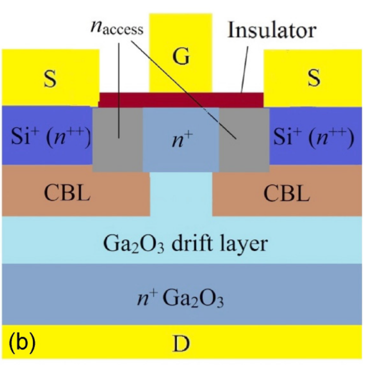

FIG. 10. Vertical-type MOSFET designs with active regions created by ion implantation: (a) with n^{++} contact source/drain regions and CBL region doped by N^+ or Mg^+; (b) the same as (a), but with access area.

method [Fig. 10(a)]. The conditions for Mg^+ implantation[114] were as follows: $E = 560$ keV and $D = 8 \times 10^{12}$ cm^{-2}; the conditions for N^+ implantation were the same as in Ref. 50. The magnesium and nitrogen concentrations at a depth of 0.5–0.6 μm were 2×10^{17} and 1.5×10^{18} cm^{-3}, respectively. After the activation annealing for 30 min in N_2 at 1000 °C for Mg^+ (Ref. 114) and 1100 °C for N^+,[115] these impurities served as compensating acceptors, and significantly reduced the electron concentration in CBL. Transistor structures with CBL formed by Mg^+ implantation were characterized by a significant leakage current (exceeding 10 A/cm^2 at a voltage of 1 V). The reason for this was explained by the Mg diffusion confirmed by the SIMS. Nitrogen has a significantly lower diffusion coefficient, which makes it possible to use higher annealing temperatures required for the efficient activation of embedded ions.[115] Thus, N^+ implantation for the CBL formation is preferred. It should be noted that, according to Refs. 114 and 115, the characteristics of vertical mode MOSFETs were still inferior compared to lateral mode.

For the development of an E-mode MOSFET of vertical type,[113] in addition to the formation of n^+ channel by Si^+ implantation and n^{++} contact regions and CBL by N^+ implantation, an access region was formed that differed from the contact regions by a higher concentration of Si^+ [Fig. 10(b)]. The characteristics of the E-mode MOSFET of vertical type in Ref. 113 were also inferior to the characteristics of the MOSFET of lateral type, but the authors of Ref. 113 expected that, with improved dielectric quality and optimized doping schemes, their work promises a transformational impact. However, in Ref. 130, the record values of $V_{br} = 2633$ V and a BFOM = 280 MW cm^{-2} were demonstrated for the vertical multi-fin E-mode MOSFET among all types of power Ga_2O_3 MOSFETs, in which ion implantation was used to create ohmic contacts to source. The authors noticed the effect of postdeposition annealing at 350 °C for 1 min in N_2 to achieve a record low specific on-resistance = 5.2 mΩ cm^2 and a high channel mobility of ~130 cm^2/(V s).

Let us now consider the works in which ion implantation was used to create β-Ga_2O_3-based power SBDs. In Refs. 107 and 118, it was found that the use of implantation for the formation of high-resistance regions or GR at the anode allows reducing the reverse current and significantly increasing V_{br} in the vertical mode SBD (Fig. 11). In Ref. 107, the GR was formed by N^+ ion implantation to the 0.8 μm depth with a concentration of 1.0×10^{17} cm^{-3}. The activation annealing was carried out at 1100 °C for 30 min in an N_2 atmosphere. The GR formation increased V_{br} from 750 to 860 V. The authors used GR also to create an SBD with a field-plated electrode and found that in this case V_{br} increased from 1380 to 1430 V. In Ref. 118, Mg^+ implantation with the energy/dose ratios 50 keV/1.4×10^{14} cm^{-2}, 125 keV/2×10^{14} cm^{-2}, and 250 keV/9.8×10^{14} cm^{-2} was used to create a high-resistance region in SBD. The doping region depth was 0.8 μm, and the implanted impurity concentration was $(2–3) \times 10^{19}$ cm^{-3}. Annealing after implantation was not carried out, so the increase in resistivity was associated apparently not with the Mg acceptor properties but with the donor compensation by radiation defects. The use of high-resistance region reduced the reverse current and increased V_{br} from 500 to 1550 V.

In Ref. 119, as mentioned above, the possibility of using Ar^+ ion implantation to form both low-resistance regions under ohmic contacts and a high-resistance region at the edges of the anode was shown as well. The implantation conditions used for the ohmic

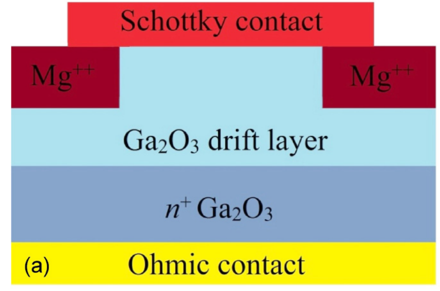

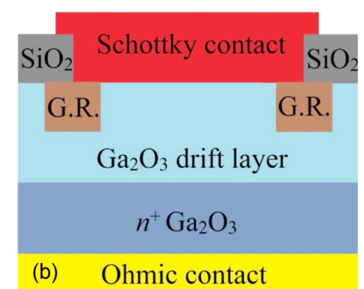

FIG. 11. SBD structures based on β-Ga_2O_3 with regions formed by N^+ or Mg^+ implantation: (a) with a high-resistance region near the anode; (b) with GR

Published under license by AVS.

TABLE III. β-Ga_2O_3-based MOSFET and SBD characteristics.

Ions	Purpose of implantation	Type of device	Substrate	V_{br} (V)	BFOM (MW cm^{-2})	I_{on}/I_{off}	ρ_c (Ω cm^2)	Reference
Si^+	Ohmic contacts	Lateral D-mode MOSFET	β-Ga_2O_3 (010)	404	—	$>10^{10}$	8.1×10^{-6}	Ref. 108
Si^+	Ohmic contacts	Lateral D-mode MOSFET	β-Ga_2O_3 (010)	415	—	$>10^{10}$	8×10^{-6}	Ref. 109
Si^+	Ohmic contacts	Lateral D-mode FP-MOSFET	UID Ga_2O_3, buffer layer	755	—	$>10^9$	—	Ref. 111
Si^+	Ohmic contacts	Lateral E-mode MOSFET	UID Ga_2O_3, buffer layer	—	—	9×10^5	7.5×10^{-6}	Ref. 126
Si^+ Mg^+	Channel, Ohmic contacts CBL	Vertical D-mode FP-MOSFET	Ga_2O_3(001)	—	—	—	—	Ref. 114
Si^+	Ohmic contacts, channel	Lateral D-mode MOSFET	UID Ga_2O_3, buffer layer	480 for "air annealing," 1340 for "fluorine annealing"	—	10^5	—	Ref. 116
		Lateral D-mode FP-MOSFET		720 for "air annealing," 2360 for "fluorine annealing"	8.8			
Si^+	Ohmic contacts	Lateral D-mode FP-MOSFET	UID Ga_2O_3, buffer layer	480	50.4	10^5	4.6×10^{-3}	Ref. 117
Si^+	Ohmic contacts	Lateral SAG MOSFET	Ga_2O_3 (010)	—	—	10^8	—	Ref. 129
Si^+ N^+	Channel, Ohmic contacts, CBL	Vertical D-mode FP-MOSFET	β-Ga_2O_3 (001)	—	—	10^8	—	Ref. 115
Si^+	Ohmic contacts	Vertical multifin E-mode MOSFET	Ga_2O_3 (001)	2655	280	10^9	—	Ref. 130
Si^+	Ohmic contacts	Lateral D-mode FP-MOSFET	UID Ga_2O_3, buffer layer	2900 for $L_{GD} = 17.8$ μm; 1400 for $L_{GD} = 4.8$ μm	182 for $L_{GD} =$ 17.8 μm; 277 for $L_{GD} =$ 4.8 μm	10^9	—	Ref. 127
Si^+	Ohmic contacts	Lateral E-mode FP-MOSFET	UID Ga_2O_3, buffer layer	3000	94	10^8	—	Ref. 128
Si^+ H^+ Ar^+	Ohmic contacts Ohmic contacts Exfoliation of β-Ga2O3 thin film	Lateral D-mode and E-mode MOSFETs	β-Ga_2O_3 on SiC and Si(001); bulk Ga_2O_3	570; 605	—	10^7	—	Refs. 120 and 121
Si^+ N^+	Channel, Ohmic contacts CBL	Vertical E-mode MOSFET	β-Ga_2O_3 (001)	263	—	2×10^7	—	Ref. 113
N^+	CBL	SBD	Ga_2O_3 (001)	860 for GR, 1430 for GR and FP electrode	150 for GR, 400 for GR and FP electrode	—	—	Ref. 107
Mg^+	GR	SBD	β-Ga_2O_3 (001)	1550	470	—	—	Ref. 118
Ar^+	Edge termination	SBD	β-Ga_2O_3 (001)	451	61.5	—	—	Ref. 119

Published under license by AVS.

contacts formation were the following: $E = 50$ keV and $D = 2.5 \times 10^{14}$ cm^{-2}. Annealing after irradiation was carried out at $T_{ann} = 950$ °C for 60 min in an N_2 atmosphere. To form the high-resistance region, two irradiation doses of 5×10^{14} and 1×10^{16} cm^{-2} were used, and annealing was performed at $T_{ann} = 400$ °C for 60 s in an N_2 atmosphere too. Increasing the dose led to an increase in V_{br} from 252 to 451 V. These devices demonstrated thermal stability of characteristics in the range from room temperature to 150 °C. Theoretical calculations aimed to reveal the role of defects formed upon Ar^+ irradiation are presented in Ref. 131.

The characteristics of β-Ga_2O_3-based MOSFETs and SBDs processed by ion implantation are summarized in Table III. The developed devices demonstrate high breakdown voltages, low leakage currents, low resistance of ohmic contacts, and stability of parameters in a wide temperature range. It is remarkable that almost every new publication reports new achievements in terms of device characteristics improvement. Apparently, the use of ion implantation has not yet reached the limits of its capabilities in improving the characteristics of these devices.

B. Solar-blind UV detectors

Photodetectors with selective sensitivity to UV radiation with $\lambda \leq 280$ nm are commonly called "solar-blind," as they can function in sunlight conditions.[131] They find applications in various fields, such as detection of laser UV radiation, detection of cruise missile tracks, investigations of the Earth's atmosphere (e.g., detection of ozone holes), astrophysics, space investigations, biology, and medicine.

Solar-blind UV detectors should have high values of photosensitivity R_{ph}, detectivity D_{ph}, high performance, and low dark current I_d. The R_{ph} value is determined from the expression

$$R_{ph} = (I - I_d)/P, \tag{3}$$

where I is the total current when detector is exposed to radiation and P is the radiation power. The detectivity D_{ph} characterizes the ability of device to detect small UV signals and is determined by the ratio[132]

$$D_{ph} = [S/(2qI_d)]^{1/2} \times R_{ph}, \tag{4}$$

where S is the effective area of the photodetector and q is the electron charge. The performance of detector is characterized by the time of photoresponse under pulsed radiation.

Recently, a fairly large number of articles have appeared devoted to the research and development of solar-blind photodetectors based on β-Ga_2O_3.[131,132] Most attention is paid to the detectors of metal/β-Ga_2O_3/metal (Me/β-Ga_2O_3/Me) type, where the metal is used to create an ohmic contact or a Schottky barrier. UV detectors with ohmic contacts are characterized by high sensitivity, but at the same time, they have high values of the dark current.[131] The Schottky barrier detectors have lower dark currents and better response times due to the presence of the barrier electric field; however, they tend to have lower sensitivity than devices with ohmic contacts. It should be noted that high sensitivity is not always the main characteristic; for some applications, high performance is more important.

So far, only a few works have been devoted to the use of ion implantation for the creation and modification of the β-Ga_2O_3-based UV detectors properties. In Ref. 134, a β-Ga_2O_3 layer epitaxially grown by the MOCVD method on a sapphire (0001) substrate was implanted by Si^+ with an energy of 30 keV and a dose of 1×10^{15} cm^{-2}, after which the samples were annealed at 900 °C for 30–120 s in an Ar atmosphere. The depth corresponding to the maximum concentration of implanted ions was 25 nm. Si^+ implantation and an increase in the annealing duration from 30 to 90 s led to a significant decrease in the surface resistance of the film. Ti/Au films were used as ohmic contacts. The R_{ph} value of the structures upon exposure to UV radiation with $\lambda = 254$ nm was 1.45 A/W. The samples response was characterized by significant inertia due to the presence of a deep level in the β-Ga_2O_3 bandgap. Unfortunately, the authors did not compare the characteristics of the obtained detectors with the characteristics of detectors fabricated without Si^+ implantation. (It is worth noting that a decrease in the contact resistance due to implantation can lead to an increase in the dark current and, accordingly, a decrease in D_{ph}.)

133 was continued by the study of characteristics in a wide temperature (T) range—from room temperature to 350 °C.[134] The near-surface region of the β-Ga_2O_3 layer was implanted by Si^+ and then the samples were annealed under the conditions described above. The detectors showed stable performance over the entire studied temperature range, and at $T = 400$ °C, the Ti/Au contacts degradation occurred. An increase in the *rejection ratio* $[I_{ph}(\lambda = 254\ \text{nm})/I_{ph}(\lambda = 365\ \text{nm})]$ from 9 at room temperature to 216 at 350 °C was noted (the *rejection ratio* parameter characterizes the degree of the detector suitability for the use as a "solar-blind" detector). With an increase in T from room temperature to 350 °C, the difference between the photocurrent at $\lambda = 254$ nm and the dark current increased by about a factor of 7, and the R_{ph} value increased from 5 to 36 A/W.

In Ref. 136, the sensitivity of Ga_2O_3 nanowires synthesized employing plasma immersion ion implantation (PIII) of GaAs with $C_2H_2^+$ ions to pulsed nitrogen laser emission with a wavelength of 337 nm was studied. The lack of nanowire sensitivity to emission with i = 488 nm was noted. It is concluded that the method is promising for UV detectors and for the fabrication of integrated optical circuits.

VI. SUMMARY AND CONCLUSIONS

More than half a century history of research and development in the field of semiconductor electronics shows that technologies relevant to industrial application can hardly do without ion implantation due to its many advantages. This fully applies to the case of Ga_2O_3 as a material for advanced electronic and optoelectronic devices. Hence, it follows that research on ion implantation of this semiconductor should be given a scale comparable to those of the well-developed "classical" semiconductors.

Comprehensive considerations of all the aspects in this field are beyond the scope of the present review. Here, the topics and aspects that seem to be the most important are considered.

To date, gallium oxide-based MOSFET devices for power electronics have been *developed*. Such devices can serve as a basis for

Published under license by AVS.

the development of *integrated* circuits operating at high temperatures. In order to meet the requirements for high performance and high degree of integration, a microminiaturization of circuits is necessary—decreasing the sizes of the active and passive regions. From this point of view, ion implantation is the most appropriate technique. However, as experience in the development of silicon integrated circuits shows, further extensive studies are required to implement this task. Among them are problems such as super-shallow doping (by implantation of low-energy ions), studying the regularities of radiation-stimulated diffusion, and finding innovative ways to suppress it (by co-implantation of two and more impurities, irradiation with molecular and cluster ions, use of impurity gettering, etc.). Additional research is also required in the field of "defect engineering"—the regularities of accumulation and annealing of radiation defects, the interaction of impurities and defects, the effect of elastic stresses on diffusion, the influence of crystal surface and its orientation on the distribution of implanted atoms, etc. These problems are either not yet investigated for Ga_2O_3 or their study is in its infancy.

One of the significant drawbacks of Ga_2O_3, limiting its application, is the difficulty of producing *p*-type conductivity. This is due to the fundamental features of the energy structure of this material at the conditions close to thermodynamic equilibrium. A promising way to solve this problem is to realize nonequilibrium but relatively stable (metastable) states by means of ion implantation. Perhaps, such an approach (using ion implantation), as the introduction of a "third player" into the game (the first two "players" are the semiconductor matrix and an impurity or a defect), would also be fruitful. The third "player" can be, for example, a surface, the role of which increases in the case of using low-energy ions or new ion-synthesized phases, including nanocrystals and interfaces. Ion synthesis of ternary compounds with the aim of modifying the energy structure of a semiconductor is also a promising area of research.

All these problems require not only extensive experimental research but also the intensification of theoretical developments.

Although this review refers to the β-phase of Ga_2O_3, possible applications of gallium oxide are not limited to this phase. Therefore, it is of interest to synthesize epitaxial layers of the α-phase (with a wider bandgap than the β-phase). The problem with ion implantation of the α-phase would arise in connection with the lower thermal stability of this phase.

Further research in the area of Ga_2O_3 ion implantation is very important from both scientific and practical points of view.

ACKNOWLEDGMENTS

The study was supported by the BRICS project funded by Russian Foundation for Basic Research (Grant No. 19-57-80011), Department of Science and Technology (DST/IMRCD/BRICS/Pilot Call 3/Ga2O3 /2019), and Conselho Nacional de Desenvolvimento Científico e Tecnológico (CNPq—Brazil). D.G. acknowledges the Lobachevsky University competitiveness program in the frame of 5-100 Russian Academic Excellence Project. A.N. acknowledges the support of the President of the Russian Federation fellowship.

DATA AVAILABILITY

The data that support the findings of this study are available from the corresponding author upon reasonable request.

REFERENCES

[1]A. K. Saikumar, S. D. Nehate, and K. B. Sundaram, ECS J. Solid State Sci. Technol. **8**, Q3064 (2019).
[2]J. Kim, S. J. Pearton, C. Fares, J. Yang, F. Ren, S. Kim, and A. Y. Polyakov, J. Mater. Chem. C **7**, 10 (2019).
[3]S. J. Pearton, J. Yang, P. H. Cary, F. Ren, J. Kim, M. J. Tadjer, and M. A. Mastro, Appl. Phys. Rev. **5**, 011301 (2018).
[4]S. J. Pearton, F. Ren, M. Tadjer, and J. Kim, J. Appl. Phys. **124**, 220901 (2018).
[5]M. Razeghi *et al.*, Proc. SPIE **10533**, 105330R (2018).
[6]M. A. Mastro, A. Kuramata, J. Calkins, J. Kim, F. Ren, and S. J. Pearton, ECS J. Solid State Sci. Technol. **6**, P356 (2017).
[7]S. I. Stepanov, V. I. Nikolaev, V. E. Bougrov, and A. E. Romanov, Rev. Adv. Mater. Sci. **44**, 63 (2016).
[8]W. Hohenberg and P. Kohn, Phys. Rev. **136**, B864 (1964).
[9]W. Kohn and L. J. Sham, Phys. Rev. **140**, A1133 (1965).
[10]P. Deák, Q. Duy Ho, F. Seemann, B. Aradi, M. Lorke, and T. Frauenheim, Phys. Rev. B **95**, 075208 (2017).
[11]S. J. Clark and J. Robertson, Phys. Rev. B **82**, 085208 (2010).
[12]X. Zheng, A. J. Cohen, P. Mori-Sánchez, X. Hu, and W. Yang, Phys. Rev. Lett. **107**, 026403 (2011).
[13]J. Heyd, G. E. Scuseria, and M. Ernzerhof, J. Chem. Phys. **118**, 8207 (2003).
[14]A. V. Krukau, O. A. Vydrov, A. F. Izmaylov, and G. E. Scuseria, J. Chem. Phys. **125**, 224106 (2006).
[15]J. B. Varley, H. Peelaers, A. Janotti, and C. G. Van De Walle, J. Phys.: Condens. Matter **23**, 334212 (2011).
[16]J. B. Varley, A. Janotti, C. Franchini, and C. G. Van De Walle, Phys. Rev. B **85**, 081109(R) (2012).
[17]J. B. Varley, J. R. Weber, A. Janotti, and C. G. Van De Walle, Appl. Phys. Lett. **97**, 142106 (2010).
[18]J. P. Perdew, K. Burke, and M. Ernzerhof, Phys. Rev. Lett. **77**, 3865 (1996).
[19]K. Irmscher, Z. Galazka, M. Pietsch, R. Uecker, and R. Fornari, J. Appl. Phys. **110**, 063720 (2011).
[20]Z. Zhang, E. Farzana, A. R. Arehart, and S. A. Ringel, Appl. Phys. Lett. **108**, 052105 (2016).
[21]M. E. Ingebrigtsen, A. Y. Kuznetsov, B. G. Svensson, G. Alfieri, A. Mihaila, U. Badstübner, A. Perron, L. Vines, and J. B. Varley, APL Mater. **7**, 022510 (2019).
[22]T. Zacherle, P. C. Schmidt, and M. Martin, Phys. Rev. B **87**, 235206 (2013).
[23]L. Dong, R. Jia, B. Xin, B. Peng, and Y. Zhang, Sci. Rep. **7**, 40160 (2017).
[24]A. Kyrtsos, M. Matsubara, and E. Bellotti, Appl. Phys. Lett. **112**, 032108 (2018).
[25]J. R. Ritter, J. Huso, P. T. Dickens, J. B. Varley, K. G. Lynn, and M. D. McCluskey, Appl. Phys. Lett. **113**, 052101 (2018).
[26]Q. D. Ho, T. Frauenheim, and P. Deák, J. Appl. Phys. **124**, 145702 (2018).
[27]T. Gake, Y. Kumagai, and F. Oba, Phys. Rev. Mater. **3**, 44603 (2019).
[28]A. T. Neal *et al.*, Appl. Phys. Lett. **113**, 062101 (2018).
[29]J. L. Lyons, Semicond. Sci. Technol. **33**, 05LT02 (2018).
[30]H. Peelaers, J. L. Lyons, J. B. Varley, and C. G. Van De Walle, APL Mater. **7**, 022519 (2019).
[31]Y. Wei, X. Li, J. Yang, C. Liu, J. Zhao, Y. Liu, and S. Dong, Sci. Rep. **8**, 10142 (2018).
[32]Y. Wang *et al.*, Sci. Rep. **8**, 18075 (2018).
[33]A. M. Stoneham, J. Gavartin, A. L. Shluger, A. V. Kimmel, D. Mũoz Ramo, H. M. Rønnow, G. Aeppli, and C. Renner, J. Phys.: Condens. Matter **19**, 255208 (2007).
[34]H. J. Von Bardeleben, S. Zhou, U. Gerstmann, D. Skachkov, W. R. L. Lambrecht, Q. D. Ho, and P. Deák, APL Mater. **7**, 022521 (2019).

Published under license by AVS.

[35]A. Kyrtsos, M. Matsubara, and E. Bellotti, Phys. Rev. B **95**, 245202 (2017).
[36]D. B. Williams and C. B. Carter, *Transmission Electron Microscopy: A Textbook for Materials Science* (Springer, New York, 2009).
[37]J. E. Castle, in *Practical Surface Analysis by Auger and X-ray Photoelectron Spectroscopy*, edited by D. Briggs and M. P. Seah (Wiley, Chichester, 1983).
[38]P. Van Der Heide, *Secondary Ion Mass Spectrometry: An Introduction to Principles and Practices* (Wiley, New York, 2014).
[39]E. Bøgh, Can. J. Phys. **46**, 653 (1968).
[40]L. Meyer, Phys. Status Solidi B **44**, 253 (1971).
[41]H. J. Whitlow, Nucl. Instrum. Methods Phys. Res., Sect. B **47**, 477 (1990).
[42]E. B. Yakimov, A. Y. Polyakov, N. B. Smirnov, I. V. Shchemerov, J. Yang, F. Ren, G. Yang, J. Kim, and S. J. Pearton, J. Appl. Phys. **123**, 185704 (2018).
[43]D. V. Lang, J. Appl. Phys. **45**, 3023 (1974).
[44]X. Zhang, J. Hu, Y. Wu, and F. Lu, J. Phys. D: Appl. Phys. **42**, 145401 (2009).
[45]A. Blondeel and P. Clauws, Mater. Sci. Eng. B **71**, 233 (2000).
[46]K. Sasaki, M. Higashiwaki, A. Kuramata, T. Masui, and S. Yamakoshi, Appl. Phys. Express **6**, 086502 (2013).
[47]R. Sharma, M. E. Law, C. Fares, M. Tadjer, F. Ren, A. Kuramata, and S. J. Pearton, AIP Adv. **9**, 085111 (2019).
[48]M. J. Tadjer *et al.*, ECS J. Solid State Sci. Technol. **8**, Q3133 (2019).
[49]R. Sharma *et al.*, J. Vac. Sci. Technol. B **37**, 051204 (2019).
[50]M. H. Wong, C. H. Lin, A. Kuramata, S. Yamakoshi, H. Murakami, Y. Kumagai, and M. Higashiwaki, Appl. Phys. Lett. **113**, 102103 (2018).
[51]J. P. John and M. E. Law, Appl. Phys. Lett. **62**, 1388 (1993).
[52]S. Solmi, A. Armigliato, and F. Baruffaldi, J. Mater. Res. **6**, 2353 (1991).
[53]F. Wittel and S. Dunham, Appl. Phys. Lett. **66**, 1415 (1995).
[54]S. Solmi, S. Valmorri, and R. Canteri, J. Appl. Phys. **77**, 2400 (1995).
[55]T. Onuma, S. Fujioka, T. Yamaguchi, M. Higashiwaki, K. Sasaki, T. Masui, and T. Honda, Appl. Phys. Lett. **103**, 041910 (2013).
[56]Y. Tomm, J. M. Ko, A. Yoshikawa, and T. Fukuda, Solar Energy Mater Solar Cells **66**, 369 (2001).
[57]K. Tetzner, A. Thies, B. T. Eldad, F. Brunner, G. Wagner, and J. Würfl, Appl. Phys. Lett. **113**, 172104 (2018).
[58]S. Luan, L. Dong, X. Ma, and R. Jia, J. Alloys Compd. **812**, 152026 (2020).
[59]K. Lorenz *et al.*, Proc. SPIE **8987**, 89870M (2014).
[60]M. Peres, K. Lorenz, E. Alves, E. Nogales, B. Méndez, X. Biquard, B. Daudin, E. G. Víllora, and K. Shimamura, J. Phys. D: Appl. Phys. **50**, 325101 (2017).
[61]M. Peres, E. Nogales, B. Mendez, K. Lorenz, M. R. Correia, T. Monteiro, and N. Ben Sedrine, ECS J. Solid State Sci. Technol. **8**, Q3097 (2019).
[62]E. Nogales, J. A. García, B. Méndez, J. Piqueras, K. Lorenz, and E. Alves, J. Phys. D: Appl. Phys. **41**, 065406 (2008).
[63]E. Nogales, P. Hidalgo, K. Lorenz, B. Méndez, J. Piqueras, and E. Alves, Nanotechnology **22**, 285706 (2011).
[64]A. Gonzalo, E. Nogales, K. Lorenz, E. G. Víllora, K. Shimamura, J. Piqueras, and B. Méndez, J. Lumin. **191**, 56 (2017).
[65]M. M. Islam, M. O. Liedke, D. Winarski, M. Butterling, A. Wagner, P. Hosemann, Y. Wang, B. Uberuaga, and F. A. Selim, Sci. Rep. **10**, 6134 (2020).
[66]R. J. Borg and G. J. Dienes, *An Introduction to Solid State Diffusion* (Academic, New York, 1988).
[67]S. Ahn, F. Ren, E. Patrick, M. E. Law, and S. J. Pearton, ECS J. Solid State Sci. Technol. **6**, Q3026 (2017).
[68]R. Sharma, E. Patrick, M. E. Law, S. Ahn, F. Ren, S. J. Pearton, and A. Kuramata, ECS J. Solid State Sci. Technol. **6**, P794 (2017).
[69]P. Weiser, M. Stavola, W. B. Fowler, Y. Qin, and S. Pearton, Appl. Phys. Lett. **112**, 232104 (2018).
[70]S. Hayashi, M. Goorsky, A. Noori, and D. Bruno, J. Electrochem. Soc. **153**, G1011 (2006).
[71]M. E. Liao, Y. Wang, T. Bai, and M. S. Goorsky, ECS J. Solid State Sci. Technol. **8**, P673 (2019).
[72]J. F. Ziegler, M. D. Ziegler, and J. P. Biersack, Nucl. Instrum. Methods Phys. Res., Sect. B **268**, 1818 (2010).
[73]E. Wendler, E. Treiber, J. Baldauf, S. Wolf, and C. Ronning, Nucl. Instrum. Methods Phys. Res., Sect. B **379**, 85 (2016).
[74]K. Lorenz, E. Alves, E. Wendler, O. Bilani, W. Wesch, and M. Hayes, Appl. Phys. Lett. **87**, 89870M (2005).
[75]E. Wendler, A. Kamarou, E. Alves, K. Gärtner, and W. Wesch, Nucl. Instrum. Methods Phys. Res., Sect. B **206**, 1028 (2003).
[76]N. Hecking, K. F. Heidemann, and E. Te Kaat, Nucl. Instrum. Methods Phys. Res., Sect. B **15**, 760 (1986).
[77]S. O. Kucheyev, J. S. Williams, and S. J. Pearton, Mater. Sci. Eng. R Rep. **33**, 51 (2001).
[78]S. O. Kucheyev, J. S. Williams, C. Jagadish, J. Zou, and G. Li, Phys. Rev. B **62**, 7510 (2000).
[79]P. A. Karaseov, A. Y. Azarov, A. I. Titov, and S. O. Kucheyev, Semiconductors **43**, 691 (2009).
[80]S. O. Kucheyev, A. Y. Azarov, A. I. Titov, P. A. Karaseov, and T. M. Kuchumova, J. Phys. D: Appl. Phys. **42**, 085309 (2009).
[81]A. I. Titov, P. A. Karaseov, A. Y. Kataev, A. Y. Azarov, and S. O. Kucheyev, Nucl. Instrum. Methods Phys. Res., Sect. B **277**, 80 (2012).
[82]I. López, K. Lorenz, E. Nogales, B. Méndez, J. Piqueras, E. Alves, and J. A. García, J. Mater. Sci. **49**, 1279 (2014).
[83]E. Nogales, I. López, B. Méndez, J. Piqueras, K. Lorenz, E. Alves, and J. A. García, Proc. SPIE **8263**, 82630B (2012).
[84]E. A. Anber, D. Foley, A. C. Lang, J. Nathaniel, J. L. Hart, M. J. Tadjer, K. D. Hobart, S. Pearton, and M. L. Taheri, Appl. Phys. Lett. **117**, 152101 (2020).
[85]C. Liu *et al.*, Semicond. Sci. Technol. **33**, 095022 (2018).
[86]Q. D. Ho, T. Frauenheim, and P. Deák, Phys. Rev. B **97**, 115163 (2018).
[87]L. Vines, C. Bhoodoo, H. Von Wenckstern, and M. Grundmann, J. Phys.: Condens. Matter **30**, 025502 (2018).
[88]P. D. C. King, T. D. Veal, P. H. Jefferson, J. Zúñiga-Pérez, V. Muñoz-Sanjosé, and C. F. McConville, Phys. Rev. B **79**, 035203 (2009).
[89]V. N. Brudnyĭ, N. G. Kolin, and L. S. Smirnov, Semiconductors **41**, 1011 (2007).
[90]V. N. Brudnyi, S. N. Grinyaev, and N. G. Kolin, Physica B **348**, 213 (2004).
[91]V. N. Brudnyi, S. N. Grinyaev, and V. E. Stepanov, Physica B **212**, 429 (1995).
[92]A. Y. Polyakov *et al.*, Appl. Phys. Lett. **112**, 032107 (2018).
[93]A. Y. Polyakov, N. B. Smirnov, I. V. Shchemerov, S. J. Pearton, F. Ren, A. V. Chernykh, P. B. Lagov, and T. V. Kulevoy, APL Mater. **6**, 096102 (2018).
[94]E. Chikoidze *et al.*, Mater. Today Phys. **3**, 118 (2017).
[95]A. Y. Polyakov, N. B. Smirnov, I. V. Shchemerov, D. Gogova, S. A. Tarelkin, and S. J. Pearton, J. Appl. Phys. **123**, 115702 (2018).
[96]M. Toulemonde, Nucl. Instrum. Methods Phys. Res., Sect. B **156**, 1 (1999).
[97]G. Szenes, Nucl. Instrum. Methods Phys. Res., Sect. B **116**, 141 (1996).
[98]M. Toulemonde, S. Bouffard, and F. Studer, Nucl. Instrum. Methods Phys. Res., Sect. B **91**, 108 (1994).
[99]A. Meftah, J. M. Costantini, N. Khalfaoui, S. Boudjadar, J. P. Stoquert, F. Studer, and M. Toulemonde, Nucl. Instrum. Methods Phys. Res., Sect. B **237**, 563 (2005).
[100]R. Giulian, J. B. Salazar, W. Just, D. J. Manzo, A. M. H. De Andrade, J. R. Schoffen, F. Bernardi, D. L. Baptista, and P. F. P. Fichtner, J. Phys. D: Appl. Phys. **50**, 485104 (2017).
[101]C. L. Tracy, M. Lang, D. Severin, M. Bender, C. Trautmann, and R. C. Ewing, Nucl. Instrum. Methods Phys. Res., Sect. B **374**, 40 (2016).
[102]W. Ai *et al.*, Jpn. J. Appl. Phys. **58**, 120914 (2019).
[103]M. Toulemonde, W. Assmann, C. Dufour, A. Meftah, and C. Trautmann, Nucl. Instrum. Methods Phys. Res., Sect. B **277**, 28 (2012).
[104]C. Borschel and C. Ronning, in *Ion Beam Modification of Solids*, edited by W. Wesch and E. Wendler (Springer, New York, 2016).
[105]M. Toulemonde, C. Dufour, A. Meftah, and E. Paumier, Nucl. Instrum. Methods Phys. Res., Sect. B **166**, 903 (2000).
[106]B. J. Baliga, IEEE Electron Device Lett. **10**, 455 (1989).
[107]C.-H. Lin *et al.*, IEEE Electron Device Lett. **40**, 1487 (2019).
[108]M. Higashiwaki, K. Sasaki, T. Kamimura, M. Hoi Wong, D. Krishnamurthy, A. Kuramata, T. Masui, and S. Yamakoshi, Appl. Phys. Lett. **103**, 123511 (2013).

Published under license by AVS.

[109]M. Higashiwaki, K. Sasaki, M. H. Wong, T. Kamimura, D. Krishnamurthy, A. Kuramata, T. Masui, and S. Yamakoshi, *Technical Digest—International Electron Devices Meeting (IEDM), Washington, DC, USA, December 2013* (IEEE, New York, 2013), Vol. 13, p. 707.
[110]M. H. Wong, K. Sasaki, A. Kuramata, S. Yamakoshi, and M. Higashiwaki, Appl. Phys. Lett. **106**, 032105 (2015).
[111]M. H. Wong, K. Sasaki, A. Kuramata, S. Yamakoshi, and M. Higashiwaki, IEEE Electron Device Lett. **37**, 212 (2016).
[112]M. H. Wong, K. Sasaki, A. Kuramata, S. Yamakoshi, and M. Higashiwaki, Jpn. J. Appl. Phys. **55**, 1202B9 (2016).
[113]M. H. Wong, H. Murakami, Y. Kumagai, and M. Higashiwaki, IEEE Electron Device Lett. **41**, 296 (2020).
[114]M. H. Wong, K. Goto, Y. Morikawa, A. Kuramata, S. Yamakoshi, H. Murakami, Y. Kumagai, and M. Higashiwaki, Appl. Phys. Express **11**, 064102 (2018).
[115]M. H. Wong, K. Goto, H. Murakami, Y. Kumagai, and M. Higashiwaki, IEEE Electron Device Lett. **40**, 431 (2019).
[116]Y. Lv *et al.*, Semicond. Sci. Technol. **34**, 11LT02 (2019).
[117]Y. Lv *et al.*, IEEE Electron Device Lett. **40**, 83 (2019).
[118]H. Zhou *et al.*, IEEE Electron Device Lett. **40**, 1788 (2019).
[119]Y. Gao *et al.*, Nanoscale Res. Lett. **14**, 1 (2019).
[120]W. Xu *et al.*, *Technical Digest—International Electron Devices Meeting (IEDM), San Francisco, CA, December 2019* (IEEE, New York, 2019), p. 274.
[121]Y. B. Wang *et al.*, Sci. China: Phys., Mech. Astron. **63**, 277311 (2020).
[122]K. Zeng, J. S. Wallace, C. Heimburger, K. Sasaki, A. Kuramata, T. Masui, J. A. Gardella, and U. Singisetti, IEEE Electron Device Lett. **38**, 513 (2017).
[123]P. H. Carey IV, J. Yang, F. Ren, D. C. Hays, S. J. Pearton, A. Kuramata, and I. I. Kravchenko, J. Vac. Sci. Technol. B **35**, 061201 (2017).
[124]P. H. Carey, J. Yang, F. Ren, D. C. Hays, S. J. Pearton, S. Jang, A. Kuramata, and I. I. Kravchenko, AIP Adv. **7**, 095313 (2017).
[125]M. H. Wong, Y. Nakata, A. Kuramata, S. Yamakoshi, and M. Higashiwaki, Appl. Phys. Express **10**, 041101 (2017).
[126]Y. Lv *et al.*, IEEE Electron Device Lett. **41**, 537 (2020).
[127]Y. Lv *et al.*, Phys. Status Solidi RRL **14**, 1900586 (2020).
[128]K. J. Liddy *et al.*, Appl. Phys. Express **12**, 126501 (2019).
[129]W. Li, K. Nomoto, Z. Hu, T. Nakamura, D. Jena, and H. G. Xing, *Technical Digest—International Electron Devices Meeting IEDM19, Ann Arbor, MI, June 2019* (IEEE, New York, 2019), p. 270.
[130]R. Sharma, E. E. Patrick, M. E. Law, F. Ren, and S. J. Pearton, ECS J. Solid State Sci. Technol. **8**, Q234 (2019).
[131]X. Chen, F. Ren, S. Gu, and J. Ye, Photonics Res. **7**, 381 (2019).
[132]Y. Qin *et al.*, Chin. Phys. B **28**, 018501 (2019).
[133]S. Oh, Y. Jung, M. A. Mastro, J. K. Hite, C. R. Eddy, and J. Kim, Opt. Express **23**, 28300 (2015).
[134]S. Ahn, F. Ren, S. Oh, Y. Jung, J. Kim, M. A. Mastro, J. K. Hite, C. R. Eddy, Jr., and S. J. Pearton, J. Vac. Sci. Technol. B **34**, 041207 (2016).
[135]K. C. Lo, H. Wang, H. P. Ho, and P. K. Chu, *IEEE Conference on Electron Devices and Solid-State Circuits 2007 EDSSC, Tainan, Taiwan, December 2007* (IEEE, New York, 2007), p. 1171.

Published under license by AVS.